Sensitivity study for N-NB-driven modes in JT-60U: boundary, diffusion, gyroaverage, compressibility

journal or publication title	Nuclear Fusion
volume	56
number	10
page range	106009
year	2016-08-09
URL	http://hdl.handle.net/10655/00012814

doi: http://dx.doi.org/10.1088/0029-5515/56/10/106009

Sensitivity study for N-NB-driven modes in JT-60: Boundary, diffusion, gyroaverage, compressibility

A. Bierwage[1], **Y. Todo**[2], **N. Aiba**[1] **and K. Shinohara**[3]
1 National Institutes for Quantum and Radiological Science and Technology, Rokkasho Fusion Institute, Aomori 039-3212, Japan
2 National Institute for Fusion Science, Toki, Gifu 509-5292, Japan
3 National Institutes for Quantum and Radiological Science and Technology, Naka Fusion Institute, Ibaraki 311-0193, Japan

E-mail: `bierwage.andreas@qst.go.jp`

Abstract. The sensitivity of the growth and nonlinear evolution of fast-ion-driven modes is examined with respect the choice of particle boundary conditions, diffusion coefficients, fast ion gyroradii and bulk compressibility. The primary purpose of this work is to justify the choice of parameters to be used in self-consistent long-time simulations of fast ion dynamics using global MHD-kinetic hybrid codes that include fast ion sources and collisions. The present study is conducted for a scenario based on the N-NB-driven JT-60U shot E039672, which is subject to Abrupt Large Events (ALE). We use realistic geometry, a realistic fast ion distribution, and focus on experimentally observed harmonics with low toroidal mode numbers $n = 1$, 2, 3. The use of realistic boundary conditions and finite Larmor radii for the fast ions is shown to be essential. The usual values $\mu_0\eta = \nu = \chi \sim 10^{-6} v_{A0} R_0$ used for resistivity, viscosity and thermal diffusivity, and $\Gamma = 5/3$ used for the specific heat ratio (controlling the effect of compressibility) are shown to be reasonable choices. Our method of performing parameter scans around the threshold for the onset of convective amplification is proposed as a strategy for nonlinear benchmark studies.

1. Introduction

When powerful negative-ion-based neutral beams (N-NB) were injected into high-beta JT-60U tokamak plasmas, so-called "fast frequency sweeping modes" (fast FS modes) and "abrupt large-amplitude events" (ALE) were routinely observed [1, 2, 3, 4]. Strictly speaking, these phenomena occurred during those phases of the plasma discharge, where the safety factor $q(r)$ lay between 1 and 2 in the region $0.2 \lesssim r/a \lesssim 0.6$ (with minor radius $a \approx 1$ m), where the beam ion pressure gradient is predicted to be large in JT-60U. The energetic particle modes (EPM) [5] that were shown to be responsible for these phenomena [6, 7, 8, 9] have long wavelengths with toroidal mode numbers around $n \gtrsim 1$, and frequencies f in the range 40-60 kHz. This corresponds to the frequency band occupied by shear Alfvén continua between the compressibility-induced (BAE) [10, 11, 12] and toroidicity-induced (TAE) [13, 14, 15] shear Alfvén frequency gaps:

$$\omega_{\rm BAE} \lesssim \omega \sim |k_\parallel v_{\rm A}| \lesssim \omega_{\rm TAE}; \qquad (1)$$

where $\text{Re}\{i\partial/\partial t\} \leftrightarrow \omega = 2\pi f$ is the angular frequency, $v_{\text{A}} = B/\sqrt{\mu_0 n_{\text{i}} m_{\text{i}}}$ is the Alfvén velocity, and $k_{\|} \leftrightarrow -i(\boldsymbol{B}/B) \cdot \boldsymbol{\nabla}$ is the wavenumber parallel to the magnetic field $\boldsymbol{B}$.

In order to learn more about the physical processes underlying these phenomena (e.g., the trigger mechanism for ALEs) and determine their role in burning plasmas (e.g., changes in fusion performance and current drive), work is currently underway to reproduce fast FS modes and ALEs using first-principle long-time simulations [16, 17, 18]. Since such comprehensive simulations require large computational resources and each case can take several months to complete, it is not feasible to perform extensive parameter scans in such a setup directly. Nevertheless, it is important to clarify the sensitivity of the results with respect to the simulation parameters used and to identify essential model ingredients. For this purpose, it is useful to perform conventional initial-value simulations and study the short-time response of the system starting from a pre-defined unstable equilibrium.

In this paper, we report results of such conventional initial-value simulations performed with the global nonlinear hybrid code MEGA [6, 19, 20], which is also being used for the above-mentioned long-time simulations [16, 17, 18]. We focus on experimentally observed toroidal mode numbers $n = 1$, 2 and 3, and study how their dynamics are affected by

(i) the choice made for the fast ion loss boundary,

(ii) the values of MHD diffusion coefficients,

(iii) the use of gyroaveraging to account for finite Larmor radii (FLR) of fast ions, and

(iv) the bulk plasma compressibility.

MEGA describes the bulk plasma response using the full set of magnetohydrodynamic (MHD) equations, including resistivity η, viscosity ν and thermal diffusivity χ. The values of these parameters are usually chosen to be much larger than what collisionality alone would imply. For instance, the normalized value of the collisional Spitzer resistivity is estimated to be $\hat{\eta} = \eta/(\mu_0 v_{\text{A}0} R_0) \sim (1...5) \times 10^{-9}$ in the center of the JT-60U plasma considered here (see Appendix A), whereas MEGA simulations are usually run with normalized dissipation parameters around $\hat{\eta} = \hat{\nu} = \hat{\chi} \sim 10^{-6}$.

These values are meaningful because the diffusion coefficients play two important roles. On the one hand, they are a means for the practical realization of MHD closure through the dissipation of small-scale structures that are not accurately described by the MHD model; in particular, on the scale of thermal ion Larmor radii ρ_{Li} (see Appendix A). This is also required to ensure that all structures that form during the simulation can be resolved by spatial grids with reasonable resolution. On the other hand, diffusion opens energy channels that may give rise to instabilities that are not present in reality. In simulations of high-beta plasmas such as the JT-60U scenario considered here, our main “enemies” to be evaded are resistive MHD ballooning modes (cf. Fig. 2 of Ref. [9]).

On the basis of these considerations, diffusion coefficients with normalized values around 10^{-6} are a reasonable compromise, and it is useful to clarify their effect on the mode dynamics. For this purpose, we examine in the present work how the results for our N-NB-driven JT-60U scenario are affected when the normalized resistivity $\hat{\eta}$ and viscosity $\hat{\nu}$ are varied between 10^{-7} and 10^{-5}.

Note that simulations using extended hybrid models that include kinetic thermal ion (KTI) effects [21] are presently run only in the drift-kinetic limit. That is, only the thermal ion compression is kinetic (describing sound waves and Landau damping), whereas FLR effects (in particular, radiative damping) are still being mocked up by resistive and viscous diffusion, just as in the present work. Hence, the results of our sensitivity study with respect to anomalously increased diffusion coefficients is also relevant for extended hybrid simulations of interactions between fast ions and Alfvén waves, such as those reported in Refs. [22, 23, 24].

Besides the diffusion coefficients, the full set of MHD equations used here contains another free physical parameter: the ratio of specific heats Γ. For an ideal gas, the relation between Γ and the number of degrees of freedom $N_{\rm f}$ is

$$\Gamma = 1 + 2/N_{\rm f}. \tag{2}$$

Usually, MEGA is run with $\Gamma = 5/3$, which corresponds to an ideal gas with three degrees of freedom $N_{\rm f} = 3$. In this paper, we also present results obtained with two extreme values: $\Gamma = 1$ and 3. The choice $\Gamma = 1$ ($N_{\rm f} = \infty$) gives the isothermal equation of state, which is valid for particle species whose thermal velocity $v_{\rm th} = \sqrt{2T/M}$ satisfies $|\omega| \ll |k_\parallel v_{\rm th}|$, where M is the mass. This is the case for electrons, when one considers modes in the frequency range given by Eq. (1). The choice $\Gamma = 3$ ($N_{\rm f} = 1$) gives the adiabatic equation of state, which is valid for $|\omega| \gg |k_\parallel v_{\rm th}|$. This is the case for bulk ions, which satisfy $v_{\rm th,i}^2/v_{\rm A}^2 \approx \beta_{\rm bulk}/2 \approx 1\%$ in the JT-60U plasmas of interest, where the total toroidal beta is estimated to be around $\beta = \beta_{\rm bulk} + \beta_{\rm h} \approx 3.6\%$ in the center of the plasma. It is estimated that about half of the thermal pressure is due to the fast ("hot") beam ion component, with $\beta_{\rm h} \sim 1.7\%$.

The N-NB ions in JT-60U are born at energies up to $E_0 = 400$ keV with pitch angles around $\alpha/\pi \approx 0.25$ (where $\sin\alpha \equiv v_\parallel/v$). The high-beta plasmas of interest here have a relatively weak magnetic field ($B_0 = 1.2$ T on axis), so that the Larmor radius $\rho_{\rm Lh}$ of fast ions at their birth velocity $v_0 = \sqrt{2E_0/m_{\rm i}}$ is relatively large, exceeding 10% of the low-field-side minor radius $a_{\rm lfs} \approx 0.66\,{\rm m}$:

$$\rho_{\rm Lh} = v_\perp/\omega_{\rm Lh} = \sqrt{2m_{\rm i}E_0\cos^2\alpha}/(eB_0) \approx 0.076\,{\rm m} \approx 11.5\% \times a_{\rm lfs}. \tag{3}$$

Thus motivated, we examine in the present paper also the effect of fast ion gyration by comparing results obtained in the zero-Larmor-radius (ZLR) limit and with FLR. Recently, we reported first evidence showing that, on the longer time scale of 1–10 ms, gyroaveraging plays an important role for the intermittency of $n = 1$ EPM activity in N-NB-driven JT-60U plasmas [17].

In order to characterize the effect of these simulation parameters on the nonlinear dynamics of fast-ion-driven modes, we measure the saturation amplitudes and examine how the value of each parameter affects the transition from low- to large-amplitude fluctuations. This transition is facilitated by so-called "convective amplification (CA)" of resonant Alfvén wave packets [25], which has proven to be a very useful paradigm for the study of nonlinear fast ion dynamics in N-NB-driven JT-60U plasmas. In simple terms, one may describe CA as follows: “The mode continues to grow as it follows the displaced resonant particles radially ourward.” But this should not be taken too literally. A more precise analysis of the underlying processes can be found in Refs. [8, 9].

This paper is organized as follows. A brief description of the physical model and numerical methods is given in Section 2. An overview of the nonlinear evolution of the system in the case with default parameters is given in Section 3. The effects of the fast ion loss boundary, diffusion coefficients, fast ion FLR and bulk plasma compressibility are examined in Sections 4–7. In Section 8, we summarize the results and discuss implications for comprehensive long-time simulations and nonlinear benchmark studies. The Appendices contain discussions concerning the role of diffusion coefficients for physical MHD closure, and topics related to numerical stability and convergence.

2. Physical model and numerical methods

The simulation scenario is based on JT-60U shot E039672 at 4 seconds [4]. A stationary MHD equilibrium with realistic flux surface geometry computed by MEUDAS [26] and a N-NB ion distribution F_0 computed numerically by OFMC [27] are used in order to closely resemble the experimental conditions. The values of several relevant plasma parameters are given in Table A1 in Appendix A. Radial profiles of the safety factor $q(r)$ and plasma beta $\beta(r)$ were given in Fig. 2 of Ref. [28]. Several projections of the fast ion distribution F_0 were shown in Fig. 4 of Ref. [28].

The “classical” Monte-Carlo simulations performed with OFMC include realistic sources and collisions but no MHD activity, so they tend to overestimate the fast ion pressure. In order to reduce the drive to a reasonable level, the guiding center distribution is initialized with $f_{\rm h,gc}(t = 0) = f_\beta \times F_0$. The scalar factor f_β is called “drive parameter” and can be defined as (cf. Section 4 in Ref. [9]):

$$f_\beta = \beta_{\rm h,sim}/\beta_{\rm h,class}. \tag{4}$$

The quantity $\beta_{\rm h,class} = \frac{4}{3}\int {\rm d}^3v\, EF_0/(m_{\rm i}n_{\rm i}v_{\rm A}^2)$ is the “classical” fast ion beta obtained with OFMC. For the steady-state distribution that includes the entire energy range from birth to thermalization, the beta value is $\beta_{\rm h,class}(r = 0) \approx 3.6\%$ at the plasma center. Here, we consider only fast ions with energies in the range $160\,{\rm keV} \lesssim E \lesssim 400\,{\rm keV}$, for which OFMC gives $\beta_{\rm h,class}(r = 0) \approx 1.8\%$. Our default choice for the drive parameter defined in Eq. (4) is $f_\beta = 0.7$, which implies that $\beta_{\rm h,sim}(r = 0) \approx 1.3\%$ at the beginning of the simulation. In the present study, the drive parameter will be scanned through the range $0.4 \leq f_\beta \leq 1.5$ in order to determine how our simulation parameters affect the transition from low- to large-amplitude mode activity via the onset of convective amplification (CA), which we studied previously in Refs. [8, 9]. While $\beta_{\rm h}$ is varied, the total plasma beta $\beta = \beta_{\rm bulk} + \beta_{\rm h}$ is assumed to remain fixed for simplicity.

The simulations analyzed in this work were performed using the hybrid code MEGA [6, 19], where the dynamics of the bulk plasma are described by full MHD equations that are coupled to the current density vector $\delta\boldsymbol{j}_{\mathrm{h,eff}}$ of fast ions [29]:

$$
\begin{aligned}
\frac{\partial\rho_{\mathrm{b}}}{\partial t} &= -\boldsymbol{\nabla}\cdot(\rho_{\mathrm{b}}\boldsymbol{u}) && (5)\\
\rho_{\mathrm{b}}\frac{\partial\boldsymbol{u}}{\partial t} &= -\rho_{\mathrm{b}}\boldsymbol{u}\cdot\boldsymbol{\nabla}\boldsymbol{u}-\boldsymbol{\nabla}p_{\mathrm{b}}+(\boldsymbol{j}-\boldsymbol{j}_{\mathrm{h,eff}})\times\boldsymbol{B}\\
&\quad-\left[\boldsymbol{\nabla}\times(\nu\rho_{\mathrm{b}}\boldsymbol{\nabla}\times\boldsymbol{u})+\frac{4}{3}\boldsymbol{\nabla}(\nu\rho_{\mathrm{b}}\boldsymbol{\nabla}\cdot\boldsymbol{u})\right] && (6)\\
\frac{\partial\boldsymbol{B}}{\partial t} &= -\boldsymbol{\nabla}\times\boldsymbol{E} && (7)\\
\boldsymbol{E} &= -\boldsymbol{u}\times\boldsymbol{B}+\eta(\boldsymbol{j}-\boldsymbol{j}_{\mathrm{eq}}) && (8)\\
\mu_0\boldsymbol{j} &= \boldsymbol{\nabla}\times\boldsymbol{B} && (9)\\
\frac{\partial p_{\mathrm{b}}}{\partial t} &= -\boldsymbol{\nabla}\cdot(p_{\mathrm{b}}\boldsymbol{u})-(\Gamma-1)p_{\mathrm{b}}\boldsymbol{\nabla}\cdot\boldsymbol{u}+\chi\boldsymbol{\nabla}^2p_{\mathrm{b}}\\
&\quad+\nu\rho_{\mathrm{b}}(\Gamma-1)\left[(\boldsymbol{\nabla}\times\boldsymbol{u})^2+\frac{4}{3}(\boldsymbol{\nabla}\cdot\boldsymbol{u})^2\right]\\
&\quad+\eta(\Gamma-1)(\boldsymbol{j}-\boldsymbol{j}_{\mathrm{h,eff}})\cdot(\boldsymbol{j}-\boldsymbol{j}_{\mathrm{eq}}). && (10)
\end{aligned}
$$

Here, ρ_{b} and p_{b} are the density and scalar pressure of the bulk plasma, $\boldsymbol{u}$ is the single-fluid MHD velocity vector, $\boldsymbol{B}$ and $\boldsymbol{E}$ are the magnetic and electric field vectors, and $\boldsymbol{j}$ is the total current density of the plasma, including the fast ion component. Except for $\boldsymbol{E}=\delta\boldsymbol{E}$ and $\boldsymbol{u}=\delta\boldsymbol{u}$, all fields consist of a fixed non-zero equilibrium component and a fluctuating component; for instance, $\boldsymbol{j}=\boldsymbol{j}_{\mathrm{eq}}(t=0)+\delta\boldsymbol{j}(t)$.

The effective current density of fast ion guiding centers, $\boldsymbol{j}_{\mathrm{h,eff}}=\boldsymbol{j}_{\mathrm{d}}+\boldsymbol{j}_{\mathrm{mag}}$, consists of drift and magnetization currents, which are computed from the guiding center distribution $f_{\mathrm{gc,h}}$ as

$$
\boldsymbol{j}_{\mathrm{d}}=\int\mathrm{d}^3v f_{\mathrm{gc,h}}q_{\mathrm{h}}(\boldsymbol{U}_{\mathrm{gc}}-\boldsymbol{v}_E^*),\quad \boldsymbol{j}_{\mathrm{mag}}=-\boldsymbol{\nabla}\times\int\mathrm{d}^3v f_{\mathrm{gc,h}}\mu\hat{\boldsymbol{b}}; \tag{11}
$$

where $\hat{\boldsymbol{b}}=\boldsymbol{B}/B$, $\mu=m_{\mathrm{h}}v_\perp^2/(2B)$ is the magnetic moment, and $\boldsymbol{U}_{\mathrm{gc}}-\boldsymbol{v}_E^*$ is the guiding center velocity without $\boldsymbol{E}\times\boldsymbol{B}$ drift [see Eq. (12) below].

The fast ion phase space is sampled by simulation particles, which trace the orbits of guiding centers as prescribed by the following equations of motion:

$$
\begin{aligned}
\dot{\boldsymbol{R}}_{\mathrm{gc}} &= \left(\boldsymbol{v}_\parallel^*+\boldsymbol{v}_E^*+\boldsymbol{v}_B\right)\equiv\boldsymbol{U}_{\mathrm{gc}} && (12)\\
m_{\mathrm{h}}v_\parallel\dot{v}_\parallel &= \boldsymbol{v}_\parallel^*\cdot(q_{\mathrm{h}}\boldsymbol{E}-\mu\boldsymbol{\nabla}B) && (13)\\
\dot{\mu} &= 0, && (14)
\end{aligned}
$$

with

$$
\rho_\parallel\equiv\frac{m_{\mathrm{h}}v_\parallel}{q_{\mathrm{h}}B},\quad B^*\equiv B[1+\rho_\parallel\hat{\boldsymbol{b}}\cdot(\boldsymbol{\nabla}\times\hat{\boldsymbol{b}})],\quad \boldsymbol{v}_E^*=\frac{\boldsymbol{E}\times\hat{\boldsymbol{b}}}{B^*} \tag{15}
$$

$$
\boldsymbol{v}_\parallel^*=\frac{v_\parallel}{B^*}\left(\boldsymbol{B}+\rho_\parallel B\boldsymbol{\nabla}\times\hat{\boldsymbol{b}}\right),\quad \boldsymbol{v}_B=-\frac{\mu}{q_{\mathrm{h}}B^*}\boldsymbol{\nabla}B\times\hat{\boldsymbol{b}}. \tag{16}
$$

The evolution of the fast ion guiding center distribution $f_{\mathrm{gc,h}}(\boldsymbol{Z},t)$ is represented with the full-f method, and the first-order particle-in-cell (PIC) method is used to map field

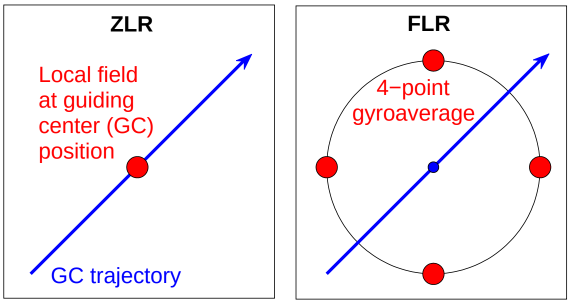

Figure 1. Zero-Larmor-radius (ZLR) limit: Electric and magnetic fields, $\boldsymbol{E}$ and $\boldsymbol{B}$, and the fast ion current density $\boldsymbol{j}_{\rm h,eff}$ are evaluated locally at the GC position. Finite Larmor radii (FLR): Fields $\boldsymbol{E}$ and $\boldsymbol{B}$ are gyroaveraged over $N_{\rm gyro}$ satellite particles (here $N_{\rm gyro} = 4$). Similarly, $\boldsymbol{j}_{\rm h,eff}$ is mapped onto the grid via the satellite particles.

values to particle positions and particle weights to field grids. Fast ion FLR effects can be taken into account using the common method of averaging over $N_{\rm gyro}$ satellite particles that are placed around the guiding center (GC) positions as illustrated in Fig. 1. MEGA acquired this feature during an upgrade performed in 2011, and it was used in benchmark activities of the International Tokamak Physics Activity (ITPA) [30, 31] as well as in recent comprehensive long-time simulations [16, 17, 18].

The simulation domain is a rectangular torus set around the wall, and it is discretized in cylindrical coordinates (R, φ, Z). The MHD equations are solved inside this domain, while suppressing fluctuations of the MHD velocity field $\delta\boldsymbol{u}$ at and beyond the plasma boundary (see Fig. 2 of Ref. [28]). Simulation particles representing fast ions are allowed to leave the plasma and follow their drift orbits through the surrounding vacuum. Particles that collide with the wall are considered lost. At the beginning of a simulation, the system is effectively self-perturbed by PIC noise, since we are using the full-f method.

A detailed discussion of resistive dissipation, its relation to continuum damping, and the choice of a suitable spatial grid (N_R, N_φ, N_Z) is given in Appendix A. Numerical convergence with respect to the number of simulation particles $N_{\rm p}$ and satellite particles $N_{\rm gyro}$ is discussed in Appendix B. Boundary smoothing and filtering methods are described and discussed in Appendix C and Appendix D. The latter also includes a discussion of the effect of nonlinear MHD mode coupling to harmonics with toroidal mode numbers up to $n = 6$, whereas the bulk of this work focuses on $n = 1$, 2 and 3.

3. Overview of mode evolution and fast ion transport for the default setup

In this section, we provide an overview of simulation results for the default scenario, around which we will perform parameter scans in the subsequent sections. The default simulation setup is as follows:

- MHD diffusion coefficients: $\hat{\eta} = \hat{\nu} = \hat{\chi} = 10^{-6}$.
- MHD specific heat ratio: $\Gamma = 5/3$.

- Fast ion drive parameter: $f_\beta = 0.7$.
- Fast ion Larmor radius: zero.
- Fast ion loss boundary: JT-60U wall.

The diffusion coefficients are normalized by the Alfvén velocity and major radius at the magnetic axis as

$$\hat{\eta} = \frac{\eta}{\mu_0 v_{\rm A0} R_0}, \quad \hat{\nu} = \frac{\nu}{v_{\rm A0} R_0}, \quad \hat{\chi} = \frac{\chi}{v_{\rm A0} R_0}. \tag{17}$$

The hats will be omitted in the following. We consider the evolution of resonantly driven modes with toroidal mode numbers $n = 1$, 2, 3, and the fast ion transport they cause.

The top row of Fig. 2 shows the evolution of the mode amplitude $A_n(t) = W_n^{1/2}(t)$ for each n. This quantity is defined as the square root of the total energy W_n contained in the fluctuations with toroidal mode number n:

$$W_{n>0} = \int \frac{{\rm d}^3x}{2} \left[\left| [\rho_{\rm b}^{1/2} \delta\boldsymbol{u}_{\rm b}]_{n>0} \right|^2 + |\delta\boldsymbol{B}_{n>0}|^2 \right]. \tag{18}$$

The middle and bottom rows of Fig. 2 show the evolution of the mode frequencies $\omega_n(t)$ and radii $r_n(t)$. These quantities identify the location of the peak of the fluctuation spectrum $|\delta\phi|_n(\omega, r)$ in the frequency-radius plane, which is computed as

$$|\delta\phi|_n(\omega, r|\vartheta_0, t_0) = \left| \int {\rm d}t\; \delta\phi_n(r, \vartheta_0, t) H(t - t_0) e^{i\omega(t-t_0)} \right| \overset{\text{peak location}}{\longrightarrow} \omega_n(t_0),\, r_n(t_0). \tag{19}$$

The toroidal harmonic $\delta\phi_n$ of the fluctuating electrostatic (ES) potential is computed from the MHD velocity vector $\delta\boldsymbol{u}$ as in Eqs. (15)–(17) in Ref. [28]. The fluctuation spectra $|\delta\phi|_n(\omega, r)$ are computed with a Hanning time window $H(t - t_0)$ of size $\Delta t_{\rm win} = 50$, using the signal at $\vartheta_0 = 0$; i.e., on the outer mid-plane of the plasma. The time is normalized by the Alfvén frequency $\omega_{\rm A0} = v_{\rm A0}/R_0$.

Figure 3 shows how the fast ion beta profile $\beta_{\rm h}(r)$ is modified by these modes. The profiles are plotted as functions of the three radial coordinates, $r = r_{\rm loc}$, $r_{\rm hfs}$ and $r_{\rm lfs}$, which were introduced in Fig. 3 of Ref. [9]. The local radius $r_{\rm loc}$ is equivalent to the poloidal magnetic flux Ψ, so it varies even along an unperturbed particle orbit due to magnetic drifts. The high-field side (HFS) and low-field side (LFS) radii $r_{\rm hfs}$ and $r_{\rm lfs}$ are equivalent to the canonical toroidal momentum P_ζ, so they are constant in the absence of fluctuations.

The results in Figs. 2 and 3 are similar to those presented in our previous papers, where we studied the convective amplification of individual modes and their effect on the fast ion profiles [8, 9]. Minor differences with the results of Ref. [8] are due to the use of a different fast ion distribution function. In Ref. [8], the entire steady-state slowing-down distribution was used. Here and in Ref. [9], only the high-energy tail (around 160–400 keV) is included. Moreover, at the time of writing Ref. [9], the multi-n simulation suffered from numerical problems causing the run to terminate prematurely. Recently, we resolved this problem by applying a smoothing procedure as described in Appendix C, which prevents the formation of spiky artifacts at the plasma boundary. The results of this stabilized multi-n simulations are presented here.

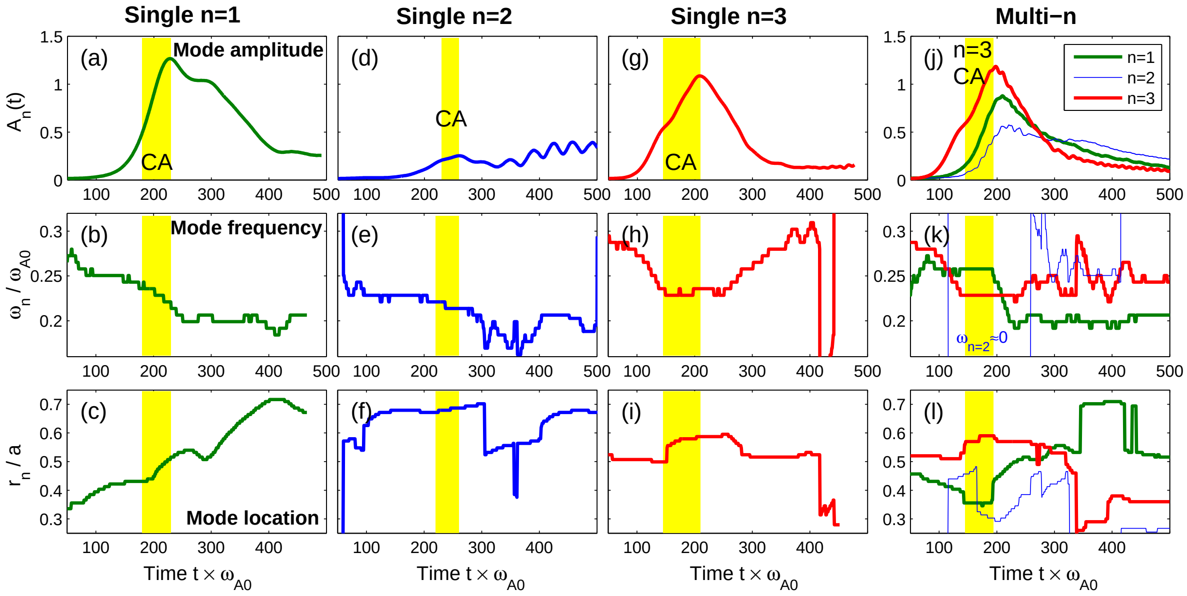

Figure 2. Overview of the evolution of $n = 1$, 2 and 3 harmonics. The top row shows the evolution of mode amplitudes $A_n(t)$, the middle row the frequencies $\omega_n(t)$ and the bottom row the radii $r_n(t)$. Results are shown for simulations with single $n = 1$ (a,b,c), $n = 2$ (d,e,f), $n = 3$ (g,h,i), and with all three harmonics (j,k,l). The shaded regions indicate intervals where convective amplification (CA) occurs.

3.1. $n = 1$ mode

This harmonic has the second-largest linear growth rate ($\gamma = 0.031$) and highest saturation amplitude [Fig. 2(a)]. During the convective amplification (CA) phase ($180 \lesssim t \lesssim 230$), its amplitude and radial location increase as $A_{n=1} = 0.5 \rightarrow 1.27$ [Fig. 2(a)] and $r_{n=1} = 0.45 \rightarrow 0.52$ [Fig. 2(c)]. In addition, there is a down-chirp of the mode frequency $\omega_{n=1} = 0.24 \rightarrow 0.215$ [Fig. 2(b)] during the CA phase. The $n = 1$ mode causes transport in the central core region $0 \lesssim r_{\rm loc} \lesssim 0.35$ [Fig. 3(a)], which corresponds to LFS radii $0.2 \lesssim r_{\rm lfs} \lesssim 0.5$ [Fig. 3(c)].

The $n = 1$ mode and its effect on fast ions were first studied in Refs. [6, 7] in a simplified setting. This was followed by a series of increasingly realistic simulations [8, 32, 33], where this global mode was found to be very robust and relatively insensitive with respect to the shaping and beta value of the plasma when the form of the shear Alfvén continuum near the toroidicity-induced gap was kept approximately the same. Both experiments [1, 2] and simulations [7] indicate that the $n = 1$ mode is responsible for the so-called fast frequency-sweeping (fast FS) modes, which are bursts of Alfvénic activity with moderate amplitudes that are commonly seen in N-NB-driven JT-60U plasmas. The $n = 1$ mode is also thought to play a key role during abrupt large events (ALE) that are seen in the same experiments. This is because of possible linear and nonlinear resonance overlaps with other harmonics, such as $n = 2$ and $n = 3$, as was shown and discussed in Refs. [28, 34, 35].

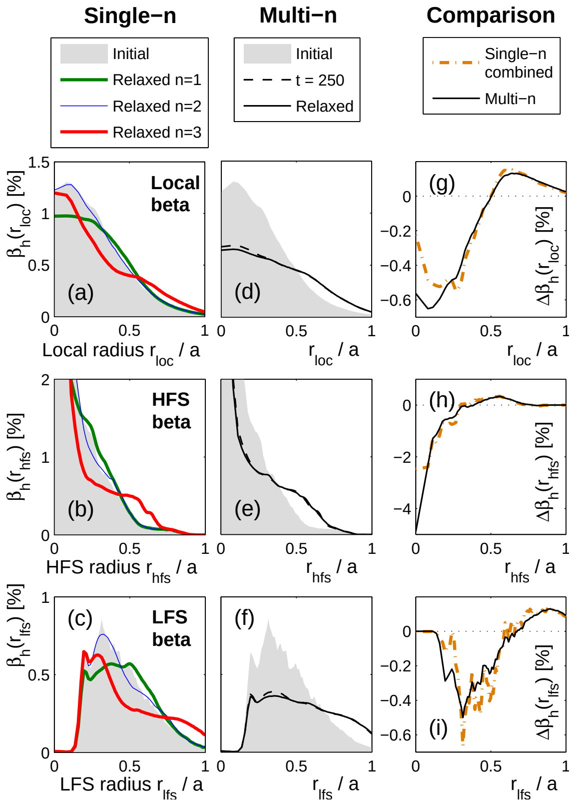

Figure 3. Comparison between initial and relaxed fast ion beta profiles. The profiles are plotted as functions of $r_{\rm loc}$ (top), $r_{\rm hfs}$ (middle), and $r_{\rm lfs}$ (bottom). The left column (a,b,c) shows the single-n simulation results. The middle column (d,e,f) shows the multi-n simulation results. In the right column (g,h,i), we plot the change in beta, $\Delta\beta_{\rm h} = \beta_{\rm h}(t_{\rm relaxed}) - \beta_{\rm h}(t=0)$, comparing the sum of the single-n simulation results ($\Delta\beta_{\rm h}^{n=1} + \Delta\beta_{\rm h}^{n=2} + \Delta\beta_{\rm h}^{n=3}$) with the result of the multi-n simulation ($\Delta\beta_{\rm h}^{n=1,2,3}$).

3.2. $n = 2$ *mode*

In the present setup, this harmonic has the lowest linear growth rate ($\gamma = 0.025$) and lowest saturation amplitude [Fig. 2(d)]. This is attributed to the mode being located in the periphery of the plasma at $r_{n=2} \approx 0.7$ [Fig. 2(f)], where the fast ion pressure gradient predicted by OFMC is relatively small. During its saturation phase, the mode undergoes only rudimental CA ($230 \lesssim t \lesssim 260$), where its amplitude and radial location increase as $A_{n=2} = 0.2 \rightarrow 0.25$ [Fig. 2(d)] and $r_{n=2} = 0.68 \rightarrow 0.69$ [Fig. 2(f)]. After saturating around $t \approx 260$, the mode continues to propagate as far as $r_{n=2} = 0.7$, while its frequency chirps down as $\omega_{n=2} = 0.22 \rightarrow 0.2$ [Fig. 2(d)]. Subsequently ($t \gtrsim 300$), pulsating $n = 2$ fluctuations with frequencies $\omega_{n=2} \lesssim 0.2$ appear near $r_{n=2} = 0.55$, which propagate to $r_{n=2} \approx 0.68$ and grow to $A_{n=2} \approx 0.35$. In the present JT-60U scenario, such pulsations are often observed in the evolution of weakly driven or decaying modes. Overall, the fluctuations of the $n = 2$ harmonic cause a small but noticeable flattening of the fast ion pressure profile near $r_{\rm lfs} \approx 0.5$ [Fig. 3(c)].

The $n = 2$ mode was first included in nonlinear multi-n simulations of JT-60U scenarios in Ref. [9] and its resonance conditions were analyzed in Section IV C of Ref. [28]. Together with other low-n harmonics, $n = 2$ is thought to play a key role during ALEs (see Section VIII of Ref. [28]). Since the $n = 2$ mode receives relatively little resonant drive in the present scenario, its dynamics will not be analyzed in detail in this paper. Its role will be limited to nonlinear MHD couplings in multi-n simulations.

3.3. $n = 3$ mode

This harmonic has the largest linear growth rate ($\gamma = 0.059$) and second-highest saturation amplitude [Fig. 2(g)]. Before the CA phase, the mode frequency chirps down as $\omega_{n=1} = 0.28 \rightarrow 0.23$ [Fig. 2(h)]. During the CA phase ($145 \lesssim t \lesssim 210$), its amplitude and radial location increase as $A_{n=3} = 0.54 \rightarrow 1.1$ [Fig. 2(g)] and $r_{n=3} = 0.5 \rightarrow 0.59$ [Fig. 2(i)]. The $n = 3$ mode causes transport in an annular (off-axis) region around $0.15 \lesssim r_{\rm loc} \lesssim 0.6$ [Fig. 3(a)], which corresponds to LFS radii $0.35 \lesssim r_{\rm lfs} \lesssim 0.8$ [Fig. 3(c)].

The $n = 3$ mode and its effect on fast ions were studied in Ref. [9]. Together with other harmonics, such as $n = 1$ and $n = 2$, the $n = 3$ mode is thought to play a key role during ALEs. This is because of the possibility of linear and nonlinear resonance overlaps, as was shown and discussed in Refs. [28, 34, 35].

3.4. Multi-n simulation

Figure 2(j,k,l) shows the results of a simulation that includes all three harmonics, $n = 1$, 2, 3. Due to its large linear growth rate and large peak amplitude, the $n = 3$ mode dominates this multi-n simulation during the interval $t \lesssim 250$. During that interval, $n = 3$ evolves almost as if the other harmonics were not present [cf., Fig. 2(g,h,i)]. After reaching its peak at $t \approx 210$, the amplitude $A_{n=3}$ decays more rapidly than the other harmonics and drops below $A_{n=1}$ and $A_{n=2}$ around $t \approx 280$ [Fig. 2(j)].

The growth rate and peak amplitude of the $n = 1$ mode are somewhat reduced compared to the single-n simulation [cf., Fig. 2(a,b,c)]. Moreover, the evolution of its radial location $r_{n=1}$ in the multi-n simulation is different, while the evolution of its frequency $\omega_{n=1}$ is similar to the single-n simulation.

The evolution of the $n = 2$ mode is entirely different from the single-n simulation [cf., Fig. 2(d,e,f)]. Its amplitude $A_{n=2}$ decays more slowly than $A_{n=1}$ and $A_{n=3}$, so that it eventually dominates for $t \gtrsim 300$ [Fig. 2(j)]. In fact, the evolution of the $n = 2$ mode seems to be dominated by MHD nonlinearities rather than direct resonant drive.

Figure 3(d,e,f) shows that the fast ion beta profile undergoes global flattening during the time interval $t \lesssim 250$, whereas only negligible profile changes occur after that time. Figure 3(g,h,i) shows that the profile change $\Delta\beta_{\rm h} = \beta_{\rm h}(t = t_{\rm relaxed}) - \beta_{\rm h}(t = 0)$ in the multi-n simulation is nearly equal to the sum of the profile changes caused by the individual harmonics in the single-n simulations. Only near the magnetic axis ($r_{\rm loc}, r_{\rm lfs} \lesssim 0.2$), the change $\Delta\beta_{\rm h}$ in the multi-n simulation is significantly larger. There, however, the change in the absolute number of particles ($\sim r \times \beta_{\rm h}(r)$) is small due to the small spatial volume.

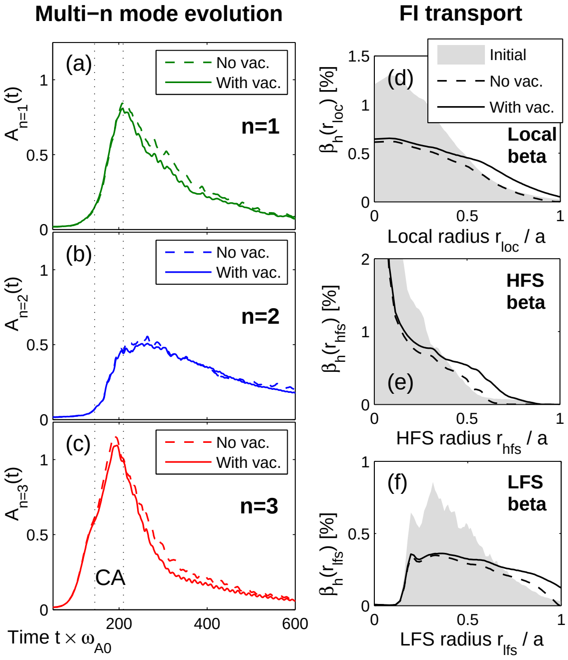

Figure 4. Role of the vacuum region in the multi-n simulation. Without vacuum, particles crossing the plasma boundary (last closed flux surface) are discarded. With vacuum, only particles hitting the wall are discarded. (a)–(c): Time traces of the mode amplitude $A_n(t)$ for $n = 1, 2, 3$ without (dash-dotted) and with vacuum region (solid). (d)–(f): Comparison between initial (shaded) and relaxed fast ion beta profiles $\beta_{\rm h}(r)$ plotted as functions of (d) $r_{\rm loc}$, (e) $r_{\rm hfs}$, and (f) $r_{\rm lfs}$.

4. Role of the vacuum region and fast ion loss boundary

One can see in Fig. 3 that the fast ion profiles can be flattened all the way into the vacuum region, but only on the low-field side [Fig. 3(c,f)]. On the high-field side [Fig. 3(b,e)], there remains a steep gradient inside the plasma, in the region $0.5 \lesssim r_{\rm hfs} \lesssim 0.7$. The location of this steep-gradient region will change if the fast ions are not allowed to travel through the vacuum region; that is, if one discards particles that traverse the plasma boundary (last closed flux surfaces), as is done in many codes used to study fast ion dynamics. The effect of imposing such an unrealistic boundary condition on the fast ions in the present scenario is shown Fig. 4 for the multi-n simulation. The left column shows the evolution of the mode amplitude $A_n(t)$ for each toroidal harmonic $n = 1$, 2 and 3. The right column shows the fast ion beta profiles $\beta_{\rm h}(r)$ as functions of $r = r_{\rm loc}$, $r_{\rm hfs}$ and $r_{\rm lfs}$. Results obtained with and without vacuum region are compared.

One can see in Fig. 4(a)–(c) that the presence of the vacuum region has a negligibly small effect on the evolution of any of the internal modes that dominate in the present simulation scenario. This is not surprising, since the initial fast ion beta profile does not extend into the vacuum, as can be seen from the shaded regions in Fig. 4(d)–(f). In contrast, the relaxed fast ion beta profiles in Fig. 4(d)–(f), which are found at the end of the instability pulses, are significantly different in the simulations with and without

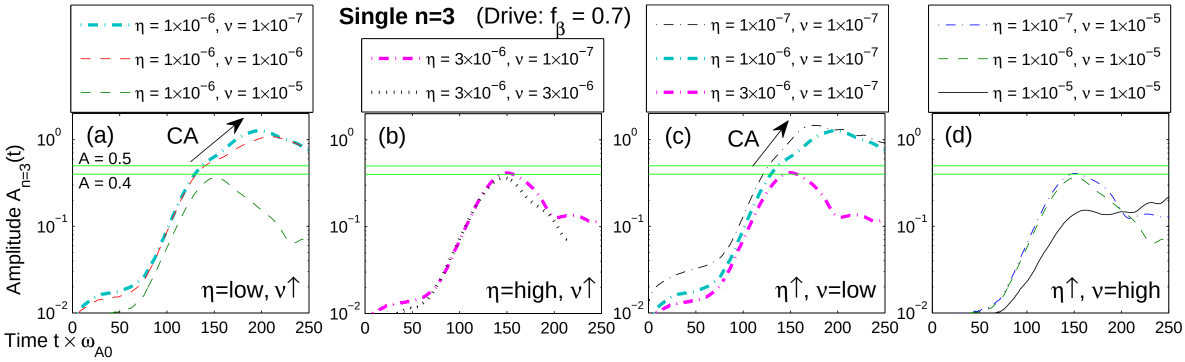

Figure 5. Effect of resistivity and viscosity on the growth and saturation level of the $n = 3$ mode. The fast ion drive parameter is fixed at $f_\beta = 0.7$. The evolution of the $n = 3$ mode amplitude $A_{n=3}(t)$ is plotted on a logarithmic scale as a function of time t and compared for four sets of parameters: (a) low resistivity $\eta = 10^{-6}$; (b) high resistivity $\eta = 3 \times 10^{-6}$; (c) low viscosity $\nu = 10^{-7}$; (d) high viscosity $\nu = 10^{-5}$. The convective amplification (CA) phase in (a) and (c) is indicated by arrows.

vacuum. For the LFS profile $\beta_\mathrm{h}(r_\mathrm{lfs})$ in Fig. 4(f), the relative difference is 10-100% in the region $r_\mathrm{lfs} \gtrsim 0.5$. For the HFS profile $\beta_\mathrm{h}(r_\mathrm{hfs})$ in Fig. 4(e), this is the case in the region $r_\mathrm{hfs} \gtrsim 0.2$; i.e., deep inside the plasma. Moreover, note that the relative smoothness of the radial cut-off in the fast ion beta profiles in Fig. 4(d)–(f) is a consequence of integration over velocity space. Locally in velocity space, the radial cut-offs are sharp.

These results suggest that the use of a realistic fast ion loss boundary may be important in long-time simulations with MHD activity, sources and collision. There, the steady-state fast ion profiles are expected to be broader, so that modes in the outer region of the plasma may also be destabilized.

5. Role of diffusion coefficients

In this section, we examine the role of resistive and viscous diffusion on the evolution of fast-ion-driven modes. We focus primarily on the $n = 3$ mode, which is the highest mode number we are usually interested in for the present JT-60U scenario, and which is therefore most strongly affected by diffusion terms. In Section 5.1, the values of η and ν are varied independently and the effect on the evolution of the mode amplitude is described. The effect of dissipation on convective amplification is studied in Section 5.2. Finally, the effect of dissipation on fast ion transport in single $n = 3$ and multi-n simulations is examined in Section 5.3.

The effect of thermal diffusivity χ is not examined explicitly here, because χ is a small parameter that directly affects only the evolution of the plasma beta, which is already a small quantity. For simplicity, χ will be set equal to either η or ν, whichever quantity is smaller.

5.1. Effect of resistivity and viscosity on growth rate and saturation level of $n = 3$ *mode*

Figure 5 shows the evolution of the $n = 3$ mode amplitude $A_{n=3}(t)$ for four sets of parameters. In Figs. 5(a) and 5(b), one can see the effect of varying viscosity ν for resistivity fixed at a lower and a higher value, respectively. Similarly, in Figs. 5(c) and 5(d), one can see the effect of varying resistivity η for viscosity fixed at a lower and a higher value, respectively.

The comparisons in Fig. 5 show that the growth rate of the fastest growing instability is essentially independent of both η and ν when their values are below 10^{-5}. Only in the last case in Fig. 5(d), where both diffusion coefficients have a relatively large value of $\eta = \nu = 10^{-5}$, the growth rate is noticeably reduced by about 40%.

The first saturation occurs at a similar amplitude in all cases, at about $A_{n=3} \approx 0.4...0.5$ as indicated by the horizontal green lines. The only exception is again the case $\eta = \nu = 10^{-5}$ in Fig. 5(d), where the first saturation occurs at a much lower level around $A_{n=3} \approx 0.15$.

The convective amplification (CA) of the $n = 3$ mode exhibits significant sensitivity with respect to both η and ν when their values are around 3×10^{-6}. In Figs. 5(a) and 5(c), where either η or ν is fixed at a relatively low value, one can clearly see how the CA phase disappears when the variable diffusion parameter is increased to 3×10^{-6} or above. In Figs. 5(b) and 5(d), there is no CA since one of the diffusion parameters is fixed at a value equal to or larger than 3×10^{-6}.

After saturation (with or without CA), the $n = 3$ mode amplitude decays in a more or less pulsating manner. The only exception is again the $\eta = \nu = 10^{-5}$ case in Fig. 5(d), where the mode resumes to grow after $t > 200$. An explanation for this behavior is given at the end of the following Section 5.2.

5.2. Convective amplification (CA) and chirping of $n = 3$ *mode*

The CA of the $n = 3$ mode was studied in detail in Ref. [9] for $\eta = \nu = \chi = 10^{-6}$. In this section, we examine how the CA as well as the frequency chirping change when the diffusion coefficients are changed, while letting $\eta = \nu = \chi$.

The left-hand side of Fig. 6 shows the evolution of (a) the $n = 3$ mode amplitude $A_{n=3}(t)$, (b) its frequency $\omega_{n=3}(t)$ and (c) its radial location $r_{n=3}(t)$ for two cases: the original case with $\eta = 10^{-6}$ (dashed lines) and a case with diffusivities reduced by one order of magnitude to $\eta = 10^{-7}$ (solid lines). For the case with weaker diffusion, the right-hand side of Fig. 6 shows snapshots of the fluctuation spectra $|\delta\phi|_{n=3}(\omega, r)$ as defined in Eq. (19). The evolution of the fluctuation spectra in the case with $\eta = 10^{-6}$ is qualitatively similar and can be seen in Fig. 7 of Ref. [9] and Fig. 5 of Ref. [35].

The linear growth phase before snapshot (A) in Fig. 6 is similar in both cases. During the first saturation phase between snapshots (A) and (B), the growth of the $n = 3$ mode slows down somewhat more rapidly in the $\eta = 10^{-6}$ case than for 10^{-7}. Apart from this, the mode frequency performs a similar downward chirp from $\omega_{n=3} \approx 0.28$ to 0.23 in both cases. As can be seen from snapshots (A)–(C) on the right-hand side of Fig. 6, the

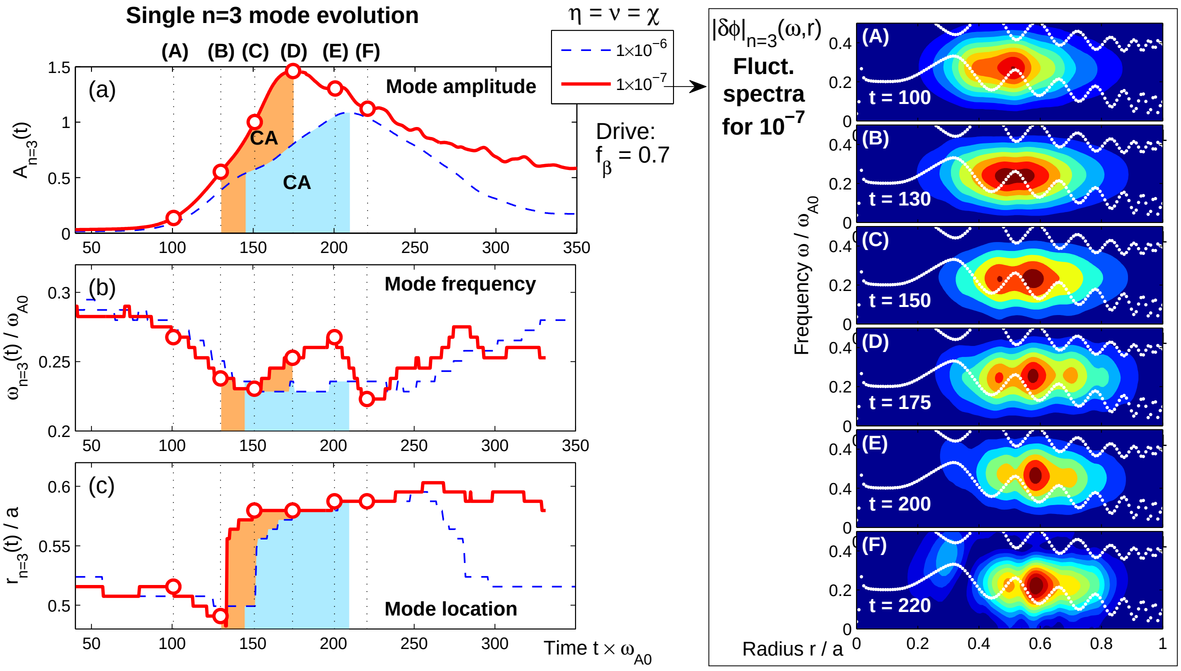

Figure 6. Effect of varying diffusion coefficients on the convective amplification (CA) of the $n = 3$ mode. The fast ion drive parameter is fixed at $f_\beta = 0.7$. Panel (a) shows the evolution of the $n = 3$ mode amplitude $A_{n=3}(t)$, (b) the frequency $\omega_{n=3}(t)$ and (c) the radial location $r_{n=3}(t)$. Two cases are compared: $\eta = \nu = \chi = 10^{-6}$ (dashed lines) and 10^{-7} (solid lines). CA phases are highlighted as shaded areas underneath the respective curves. For the 10^{-7} case, snapshots of the ES potential fluctuations $|\delta\phi|_{n=3}(\omega, r)$ are shown on the right-hand side. The times of the six snapshots labeled (A)–(F) are indicated by vertical dotted lines in panels (a)–(c).

downward chirping $n = 3$ mode splits into two components, one that propagates radially inward and one that propagates outward. Initially, the inward propagating component has a slightly larger amplitude, but eventually the outward propagating component becomes dominant. As a consequence, the time traces in Fig. 6(c) show a reduction of $r_{n=3}(t)$ from 0.52 to 0.5 around snapshot (B), followed by an abrupt increase to 0.58 during the first half of the CA phase between snapshots (B) and (C).

Between snapshot (C) and (E) in Fig. 6, the $n = 3$ mode in the $\eta = 10^{-7}$ case goes through the second half of the CA phase, saturates at its maximal amplitude, and begins to decay. During this interval, the mode frequency in Fig. 6(b) can be seen to perform a significant up-chirp from $\omega_{n=3} \approx 0.23$ to 0.27. This is followed by a rapid down-chirp around snapshot (F). This chirping appears to be facilitated by lower values of the diffusion coefficients. It can be seen in a somewhat weaker form in an intermediate case with $\eta = 3 \times 10^{-7}$ (not shown here), and it is almost absent in the $\eta = 10^{-6}$ case, as the dashed line in Fig. 6(b) shows. We believe that the physical reason for the different chirping dynamics seen during the advanced nonlinear regime (C)–(E) may be clarified through an orbit-based resonance analysis [35]. However, this goes beyond the scope of the present sensitivity study.

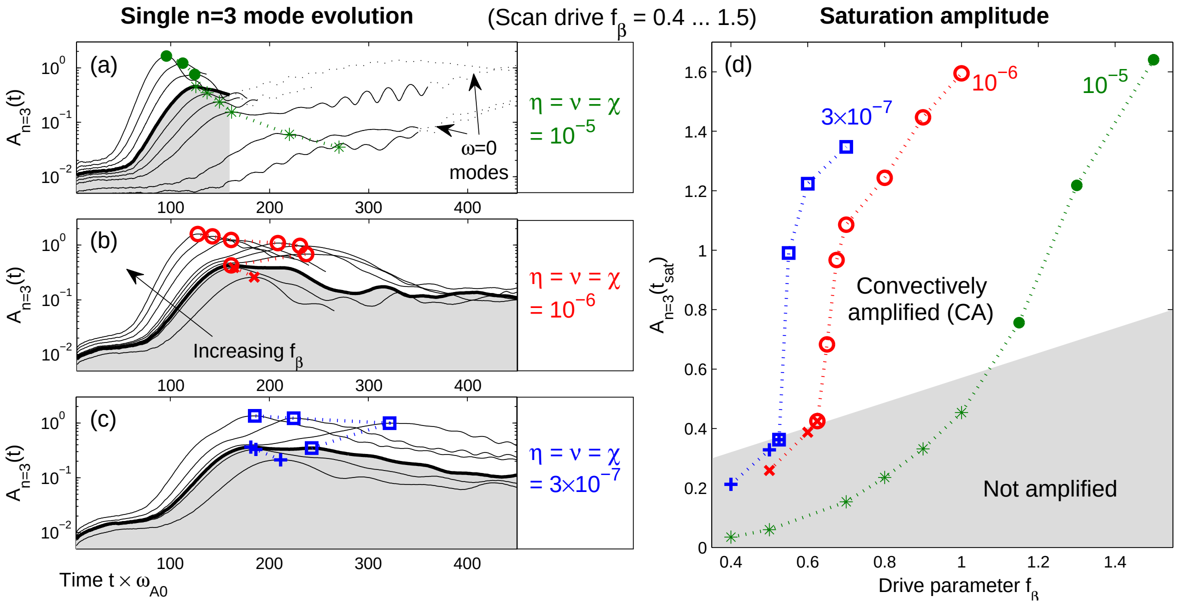

Figure 7. Effect of varying diffusion coefficients on the transition from weak to strong $n = 3$ mode activity through the onset of convective amplification (CA). Panels (a)–(c) show the individual time traces of the $n = 3$ mode amplitude $A_{n=3}(t)$ for different values of the drive parameter f_β and dissipation coefficients $\eta = \nu = \chi$. The saturation amplitudes $A_{n=3}(t_{\rm sat})$ in each case are plotted in panel (d) as functions of f_β. Shaded areas indicate cases that lie below or at the threshold for the onset of CA.

In Fig. 6 of Ref. [9], we have demonstrated that the onset of CA causes a relatively abrupt transition from weak to strong $n = 3$ mode activity when the drive parameter f_β defined in Eq. (4) is increased past a certain threshold. For the original case with $\eta = 10^{-6}$, the threshold is about $f_\beta^{\rm crit} \approx 0.625$ and the results showing this are reproduced once more in Fig. 7(b) and 7(d), although with a larger number of simulation particles (here $N_{\rm p} = 28 \times 10^6$ instead of 8×10^6 in Ref. [9]). Figure 7 shows how these results change when the strength of diffusion is increased to $\eta = 10^{-5}$ or reduced to 3×10^{-7}. The left-hand side of Fig. 7 shows the individual time traces of the $n = 3$ mode amplitude $A_{n=3}(t)$ for each case. The saturation amplitudes, $A_{n=3}(t_{\rm sat})$, which are indicated by marker symbols, are plotted once more in Fig. 7(d) as functions of f_β.

One can see in Fig. 7(d) that the use of weaker diffusion reduces the threshold for the onset of CA from $f_\beta^{\rm crit} = 0.625$ for $\eta = 10^{-6}$ to $f_\beta^{\rm crit} = 0.525$ for $\eta = 3 \times 10^{-7}$. It also seems that the threshold amplitude is slightly lower (about 10%) and the transition from weak to strong mode activity is somewhat sharper for $\eta = 3 \times 10^{-7}$. In contrast, increasing the diffusion coefficients to $\eta = 10^{-5}$ significantly increases the CA threshold to $f_\beta^{\rm crit} \approx 1.1$ and the transition becomes much more gradual.

Note that for $\eta = 10^{-5}$ the $n = 3$ mode amplitude resumes to grow at the end of each simulation. This is due to the appearance of a second instability at a larger radius, $r > 0.7$. Indeed, soon after its growth resumes, the $n = 3$ mode is dominated by a zero-frequency ($\omega = 0$) component. That portion of the time traces is plotted as dotted lines in Fig. 7(a). Eventually, a weakly growing MHD instability takes over, which is

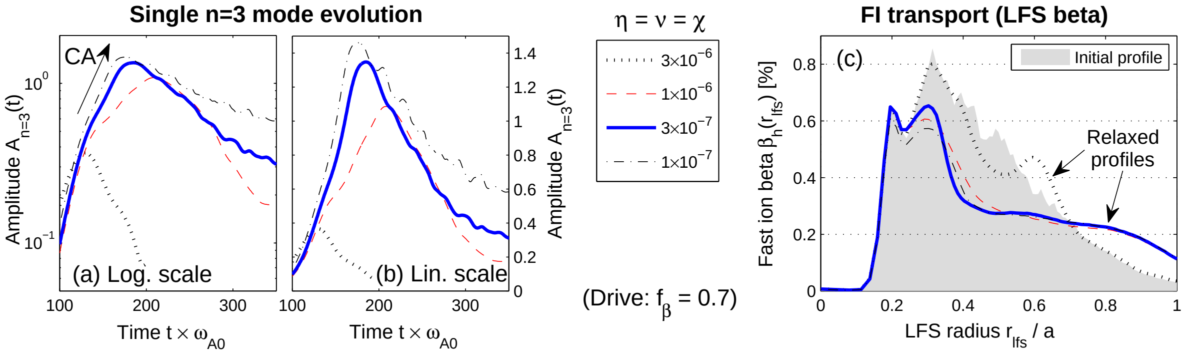

Figure 8. Effect of varying diffusion coefficients on (a,b) the decay of the resonant $n = 3$ instability and (c) the fast ion transport caused by the mode in single-n simulations with $f_\beta = 0.7$.

interpreted as an $n = 3$ resistive ballooning mode.

5.3. Decay of instabilities and relaxed fast ion profiles

When the resonant drive is exhausted, the instabilities begin to decay and the fast ion distribution settles in a relaxed state; at least, on a macroscopic scale. Results for the $n = 3$ mode in this regime are shown in Fig. 8 for several values of $\eta = \nu = \chi$ in the range $10^{-7} \leq \eta \leq 3 \times 10^{-6}$.

The evolution of the $n = 3$ mode amplitude $A_{n=3}(t)$ is shown in Figs. 8(a) and 8(b). Looking at the cases with $\eta \leq 10^{-6}$, where the instability reaches a large amplitude due to convective amplification (CA), one can see that reducing the value of the diffusion coefficients by a factor 10 reduces the overall decay rate noticeably. However, it is difficult to discuss this effect as a direct consequence of changing the strength of diffusion. As we have seen in Fig. 6 above, not only the amplitude but also the evolution of the frequency spectrum and radial mode structure are affected by the strength of diffusion. This, in turn, alters the evolution of the resonant phase space structures and fast ion distribution. As soon as the dominant resonant wave packets are located in different regions of the shear Alfvén continuum and the fast ion distribution differs, the role of the dissipation coefficients is entirely obscured.

The initial and relaxed fast ion beta profiles $\beta_{\rm h}(r)$ obtained in the $n = 3$ simulations with $10^{-7} \leq \eta \leq 3\times10^{-6}$ are compared in Fig. 8(c), where they are plotted as a function of the LFS minor radius, $r = r_{\rm lfs}$. One can see that the convectively amplified cases with $\eta \leq 10^{-6}$ all cause a similar flattening of the beta profile in the region $r_{\rm lfs} \gtrsim 0.35$ all the way into the vacuum ($r_{\rm lfs} > 1$).

An inspection of the relaxed velocity distribution for several radial slices (not shown) reveals some differences (of order 20%) in the relaxed pitch-angle distribution, which continues to evolve under the influence of low-amplitude fluctuations even hundreds of Alfvén times after the overall beta profiles $\beta_{\rm h}(r_{\rm lfs})$ have settled.

Note that the trends observed in the single-n simulation discussed above can also

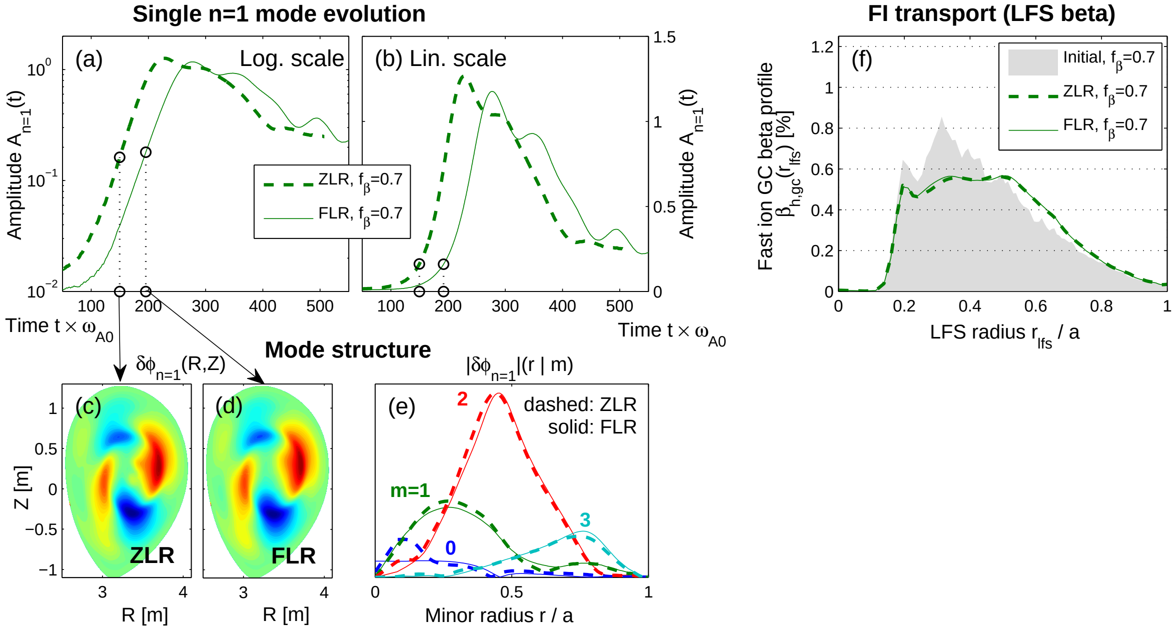

Figure 9. Effect of finite Larmor radii (FLR) of fast ions on the evolution and mode structure of the $n = 1$ mode and fast ion transport. The FLR results obtained with gyroaveraging are compared with those obtained in the zero-Larmor-radius (ZLR) limit for $f_\beta = 0.7$. (a) and (b): Evolution of the mode amplitude $A_{n=1}(t)$. (c)–(e): Linear mode structure $\delta\phi_{n=1}(R, Z)$ in the poloidal plane and radial structure $\delta\phi_{n=1}(r|m)$ of individual poloidal harmonics. (f): Initial and relaxed fast ion guiding center (GC) beta profiles $\beta_{\rm h,gc}(r_{\rm lfs})$.

be seen in the multi-n simulation results (not shown here).

6. Role of fast ion Larmor radii

In this section, we examine the role of the relatively large Larmor radii $\rho_{\rm Lh}/a_{\rm lfs} \gtrsim 10\%$ of the fast ions. For this purpose, we compare the results obtained in the zero-Larmor-radius (ZLR) and finite-Larmor-radius (FLR) limits. The diffusion coefficients and specific heat ratio are fixed at $\eta = \nu = \chi = 10^{-6}$ and $\Gamma = 5/3$.

Figures 9 and 10 show the evolution of the amplitudes $A_n(t)$ of the $n = 1$ and $n = 3$ mode in single-n simulations, as well as their linear mode structures $\delta\phi_n$ and their effect on the fast ion beta profile $\beta_{\rm h,gc}(r_{\rm lfs})$. Note that $\beta_{\rm h,gc}(r_{\rm lfs})$ is the guiding center (GC) profile; that is, it is computed without gyroaveraging even in the FLR simulation. Moreover, note that the particle noise levels in the FLR cases are lower than in the ZLR cases, because the 4 satellite particles used for gyroaveraging increase the effective number of simulation particles by a factor 4. As a consequence, the mode amplitude at the beginning of the FLR simulation is reduced by a factor $4^{-1/3} \approx 0.6$.

One can see in Figs. 9(a) and 9(b) that the evolution of the $n = 1$ mode is hardly affected by gyroaveraging. The growth rates in the ZLR and FLR simulations are essentially identical. The saturation amplitude in the FLR case is only slightly reduced

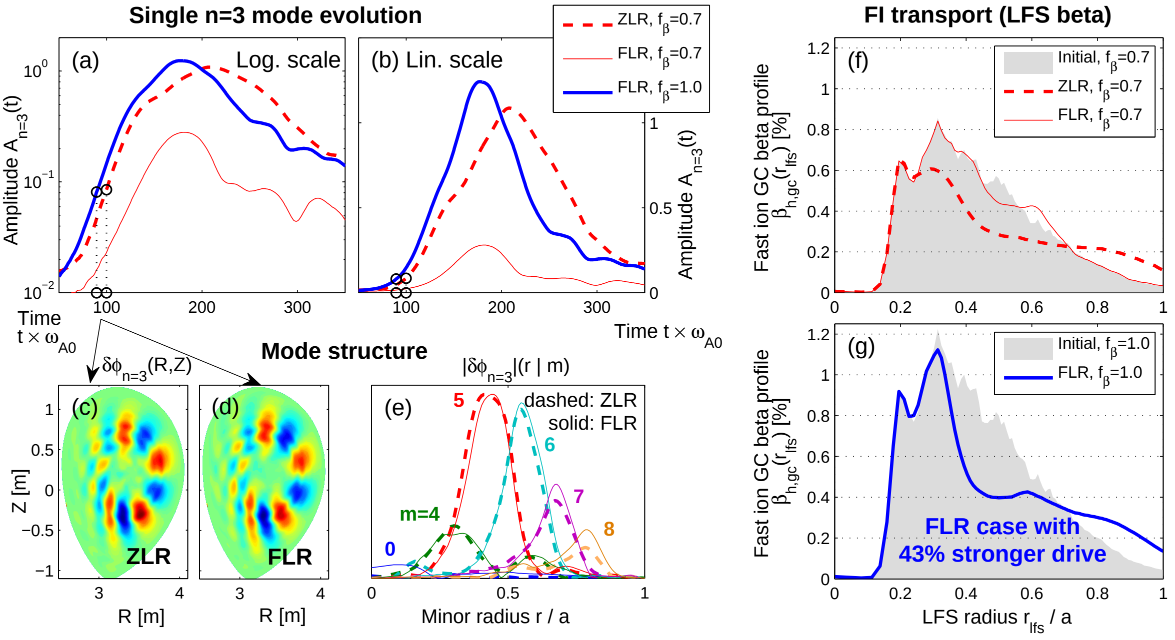

Figure 10. Effect of finite Larmor radii (FLR) of fast ions on the evolution and mode structure of the $n = 3$ mode and fast ion transport. The FLR results obtained with gyroaveraging are compared with those obtained in the zero-Larmor-radius (ZLR) limit with fast ion drive parameter $f_\beta = 0.7$. In addition, the FLR case was run once more with 43% enhanced drive ($f_\beta = 1.0$ in bold blue) for the $n = 3$ mode to reach a similar amplitude as in the ZLR limit. (a) and (b): Evolution of the mode amplitude $A_{n=3}(t)$. (c)–(e): Linear mode structure $\delta\phi_{n=3}(R, Z)$ in the poloidal plane and radial structure $\delta\phi_{n=3}(r|m)$ of individual poloidal harmonics. (f) and (g): Initial and relaxed fast ion guiding center (GC) beta profiles $\beta_{\mathrm{h,gc}}(r_{\mathrm{lfs}})$ for (f) $f_\beta = 0.7$ and (g) $f_\beta = 1.0$.

by about 7%. There is also no significant effect on the decay rate of the mode. The mode structures shown in Figs. 9(c)–(e) are hardly distinguishable, with the mode's peak in the FLR case being shifted only slightly outward by less than 1% of the minor radius. The differences in the relaxed fast ion profiles in Fig. 9(f) are also negligible.

In contrast, gyroaveraging has a substantial effect on the dynamics of the $n = 3$ mode. Figures 10(a) and 10(b) show that the growth rate in the FLR simulation is significantly reduced by about 30%. Moreover, with the default value of the drive parameter $f_\beta = 0.7$, the $n = 3$ mode in the FLR simulation does not undergo convective amplification (CA), so that it saturates at a 4 times lower amplitude and causes much less transport as can be seen in Fig. 10(f). Nevertheless, the linear mode structures shown Fig. 10(c)–(e) remain similar, with the mode's peak in the FLR case being shifted only slightly outward by less than 3% of the minor radius.

In order for the $n = 3$ mode in the FLR simulation to reach a similar amplitude as in the ZLR case, the drive must be increased by about 40%. To show this, we added in Fig. 10 another set of FLR simulation results that were obtained with drive parameter $f_\beta = 1.0$. With the enhanced drive, the $n = 3$ mode undergoes CA, grows to a large amplitude, and causes a stronger flattening of the fast ion beta profile. A comparison

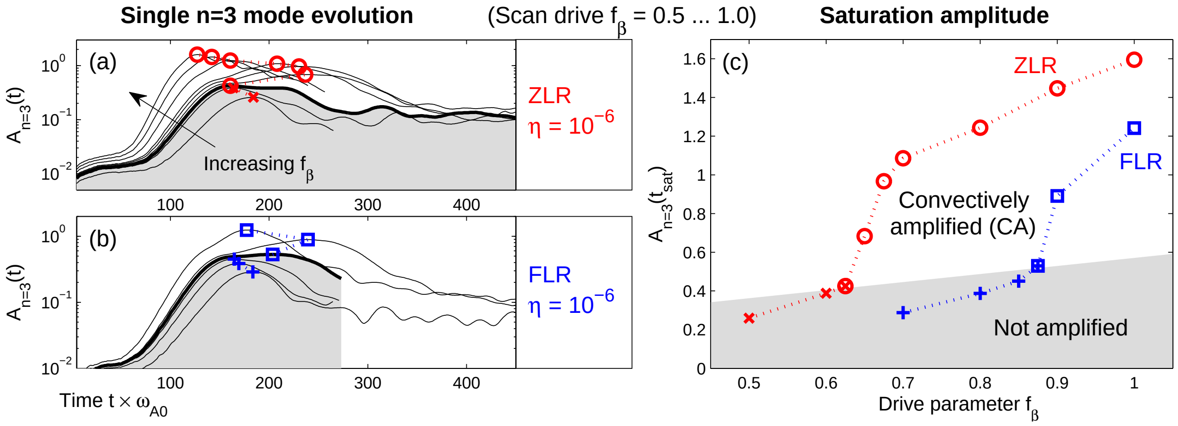

Figure 11. Effect of finite Larmor radii (FLR) of fast ions on the transition from weak to strong $n = 3$ mode activity through the onset of convective amplification (CA). Panels (a) and (b) show the individual time traces of the $n = 3$ mode amplitude $A_{n=3}(t)$ obtained in the zero-Larmor-radius (ZLR) limit and with FLR. The saturation amplitudes $A_{n=3}(t_{\rm sat})$ in each case are plotted in panel (c) as functions of f_β. Shaded areas indicate cases that lie below or at the threshold for the onset of CA.

between Figs. 10(f) and 10(g) shows that the relative drop of the fast ion beta value in the domain of the mode is similar in the ZLR case with $f_\beta = 0.7$ and in the FLR case with enhanced drive $f_\beta = 1.0$.

The results in Fig. 10 imply that the threshold for the onset of CA is significantly increased when gyroaveraging is performed. This is shown more clearly in Fig. 11(c), where we plot the saturation amplitude $A_{n=3}(t_{\rm sat})$ of the $n = 3$ mode in the ZLR and FLR simulations as a function of the drive parameter in the range $0.5 \leq f_\beta \leq 1.0$. One can see that gyroaveraging increases the threshold for the onset of CA by about 35% from $f_\beta^{\rm crit} \approx 0.65$ in the ZLR limit to $f_\beta^{\rm crit} \approx 0.875$ in the case with FLR.

On the basis of the above results we conclude that it is essential to account for FLR effects via gyroaveraging in simulations that aim at quantitative predictions or comparisons with experiments; at least, when fluctuations with toroidal mode numbers $n > 1$ play a role. In long-time simulations, even the $n = 1$ mode may be affected [17].

7. Role of bulk compressibility

In this section, we examine the effect of bulk plasma compressibility, which is controlled by the specific heat ratio Γ. For this purpose, results obtained with the default value $\Gamma = 5/3$ are compared to those obtained in the extreme limits $\Gamma = 1$ and $\Gamma = 3$. The diffusion coefficients are fixed at $\eta = \nu = \chi = 10^{-6}$. First, in Sections 7.1 and 7.2, we examine the evolution of the $n = 3$ mode and the fast ion transport it causes in the ZLR limit. In Section 7.3, we present and discuss results of multi-n simulations for toroidal harmonics $n = 1$, 2 and 3 performed with fast ion FLR (gyroavaging).

Note that none of the parameters that we have examined so far — boundary condition, diffusion and FLR — has had any influence on the macroscopic structure

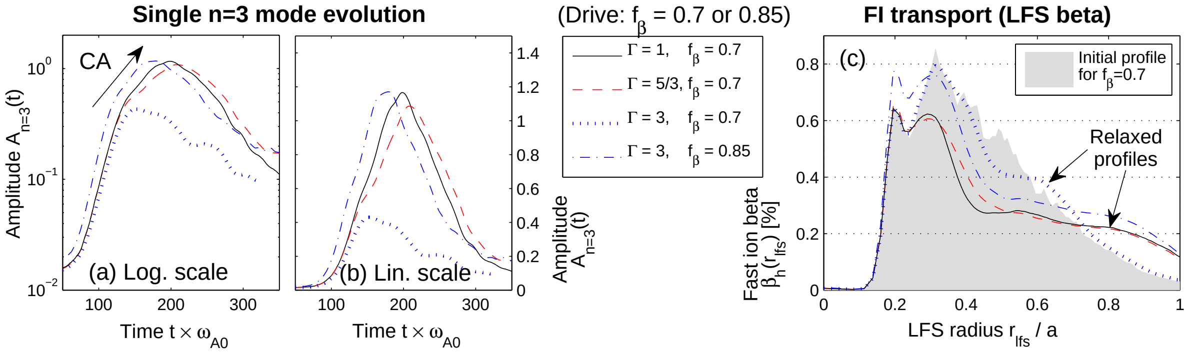

Figure 12. Effect of Γ on the evolution of the resonant $n = 3$ instability and resulting fast ion transport in single-n simulations with $f_\beta = 0.7$ and 0.85. (a) and (b): Evolution of the mode amplitude $A_{n=3}(t)$. (c): Comparison between initial (shaded) and relaxed fast ion beta profiles $\beta_{\rm h}(r_{\rm lfs})$. Here, the initial beta profile is only shown for $f_\beta = 0.7$.

of the MHD wave spectrum of the plasma. Resistivity can be said to cause an effective granulation or discretization of the shear Alfvén spectrum, but the overall structure remains unchanged. In contrast, the value of Γ has a significant impact on the structure of the shear Alfvén continua in a high-beta tokamak plasma as is considered here. In particular, it has a strong effect on the size of the compressibility-induced low-frequency gap and also causes noticeable shifts at higher frequencies around the toroidicity-induced gap as will be shown in Fig. 14 below.

7.1. Evolution of $n = 3$ mode and fast ion transport

Figure 12 shows the evolution of the amplitude $A_{n=3}(t)$ of the $n = 3$ mode in single-n simulations, as well as its effect on the fast ion beta profile $\beta_{\rm h}(r_{\rm lfs})$. One can see in Figs. 12(a) and 12(b) that, for fixed drive parameter $f_\beta = 0.7$, the growth rate is effectively insensitive to Γ; it changes by no more than 1%. With the default value of the drive parameter $f_\beta = 0.7$, the $n = 3$ mode in the "most compressible" $\Gamma = 3$ case does not undergo convective amplification (CA) and saturates at a 2–3 times lower amplitude than for $\Gamma = 5/3$ and $\Gamma = 1$. Consequently, the $n = 3$ mode in the $\Gamma = 3$ case causes significantly less fast ion transport than for the other Γ values, as is evident in Fig. 12(c).

However, with a relatively modest increase of the drive to $f_\beta = 0.85$ (dash-dotted curves in Fig. 12), CA occurs also in the $\Gamma = 3$ case. Figures 12(a) and 12(b) show that, with the enhanced drive, the peak amplitude of the $n = 3$ mode in the $\Gamma = 3$ case becomes similar to what is found in the other two cases, $\Gamma = 1$ and $\Gamma = 5/3$, with default drive $f_\beta = 0.7$. Figure 12(c) shows that the relaxed $\beta_{\rm h}(r_{\rm lfs})$ profile in the $\Gamma = 3$ case with $f_\beta = 0.85$ has a 20% larger value, but it also started from a 20% higher value than for $f_\beta = 0.7$, so the relative flattening of the fast ion beta profile is comparable.

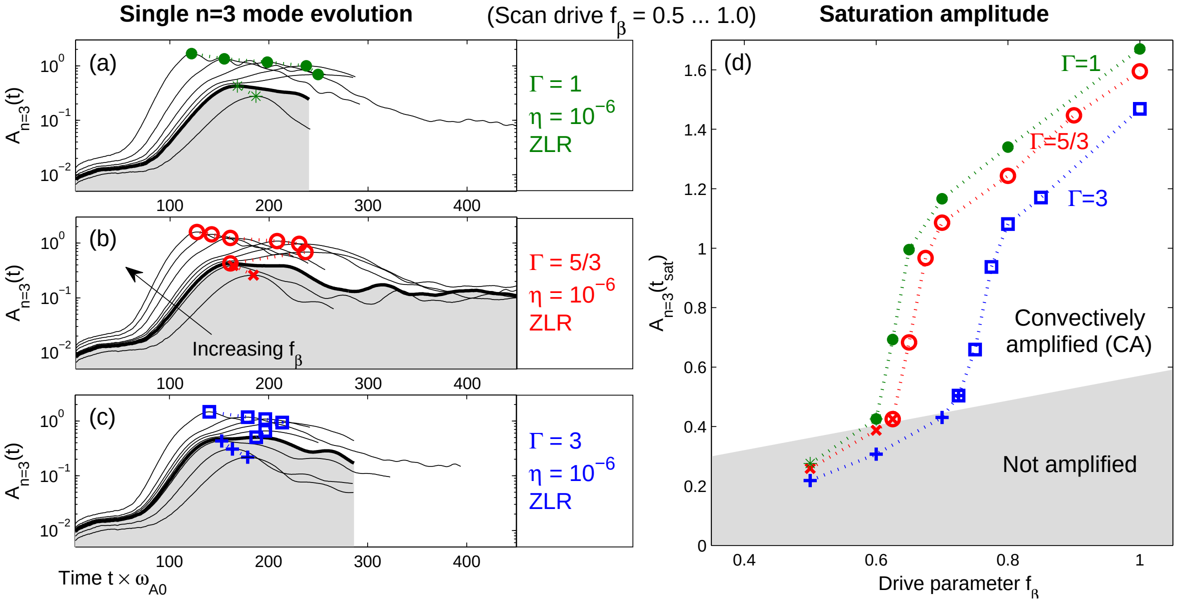

Figure 13. Effect of the specific heat ratio Γ on the transition from weak to strong $n = 3$ mode activity through the onset of convective amplification (CA). Panels (a)–(c) show the individual time traces of the $n = 3$ mode amplitude $A_{n=3}(t)$ for the three values $\Gamma = 1$, $5/3$ and 3. The saturation amplitudes $A_{n=3}(t_{\rm sat})$ in each case are plotted in panel (d) as functions of f_β. Shaded areas indicate cases that lie below or at the threshold for the onset of CA.

7.2. Convective amplification and chirping of $n = 3$ mode

The results in Fig. 12 imply that the threshold for the onset of CA increases when the value of Γ is increased. This is shown more clearly in Fig. 13(d), where we plot the saturation amplitude $A_{n=3}(t_{\rm sat})$ of the $n = 3$ mode in the simulations with $\Gamma = 1$, $5/3$ and 3 as a function of the drive parameter in the range $0.5 \leq f_\beta \leq 1.0$. One can see that, the threshold $f_\beta^{\rm crit} \approx 0.6$ for the onset of CA in the $\Gamma = 1$ case is very close to the value $f_\beta^{\rm crit} = 0.625$ found for $\Gamma = 5/3$. For $\Gamma = 3$, the threshold is near $f_\beta^{\rm crit} \approx 0.725$, which is about 15% larger than in the default case $\Gamma = 5/3$.

Let us examine in more detail the three cases of Fig. 12 that undergo CA and saturate at similar amplitudes; namely, cases $\Gamma = 1$ and $\Gamma = 5/3$ with $f_\beta = 0.7$, and case $\Gamma = 3$ with $f_\beta = 0.85$. Figure 14 shows that the frequency chirping, radial propagation, and amplification of the $n = 3$ mode proceeds in a similar manner in all three cases. In particular, the evolution of the mode location $r_{n=3}(t)$ shown in Fig. 14(c) is essentially identical in all three cases, both qualitatively and quantitatively. The evolution of the mode frequency $\omega_{n=3}(t)$ shown in Fig. 14(b) is qualitatively similar in all three cases, but there are notable quantitative differences of the order 10–20% in the value of $\omega_{n=3}$. During the linear growth phase, where snapshot (A) was taken, the mode frequencies are $\omega_{n=3} \approx 0.27, 0.28, 0.30$ for $\Gamma = 1, 5/3, 3$, respectively. At the end of the downward chirp and during the CA phase, where snapshot (B) was taken, the respective frequencies are $\omega_{n=3} \approx 0.22, 0.23, 0.25$.

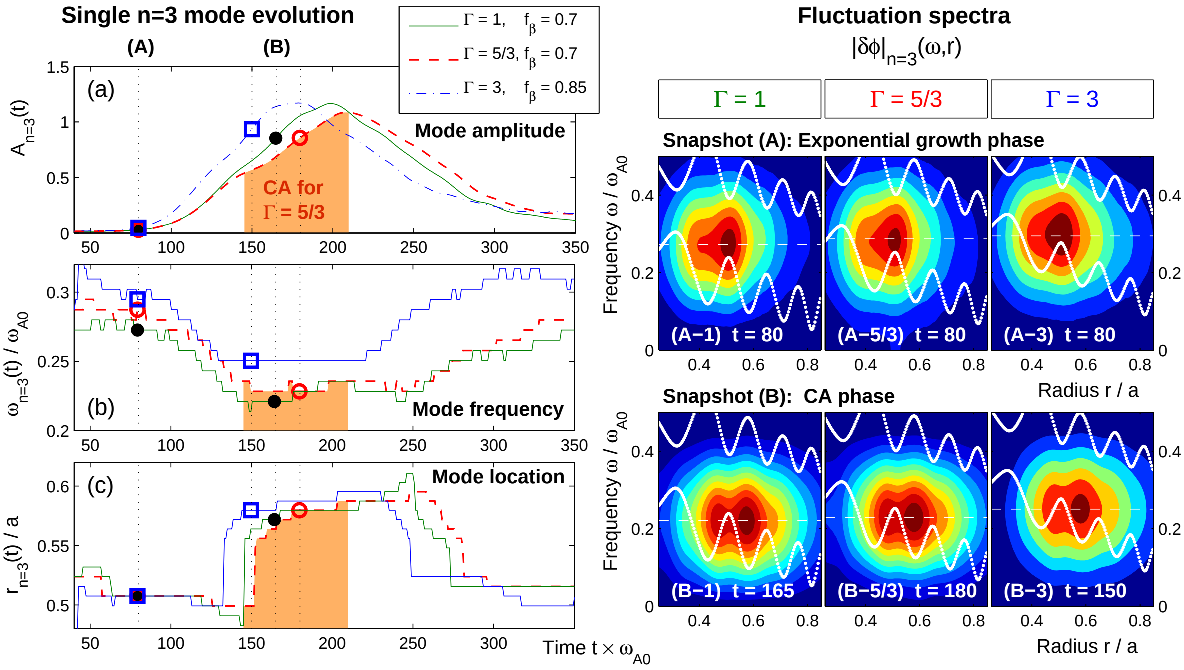

Figure 14. Effect of the specific heat ratio Γ on the convective amplification (CA) and chirping of the $n = 3$ mode. The fast ion drive parameter is $f_\beta = 0.7$ for $\Gamma = 1$ and $\Gamma = 5/3$, and somewhat increased to $f_\beta = 0.85$ for $\Gamma = 3$ (cf. Fig. 12). Panel (a) shows the evolution of the mode amplitude $A_{n=3}(t)$, (b) the frequency $\omega_{n=3}(t)$ and (c) the radial location $r_{n=3}(t)$. The CA phase of the default case with $\Gamma = 5/3$ is highlighted by shaded areas. For each case, two snapshots of the ES potential fluctuations $|\delta\phi|_{n=3}(\omega, r)$ are shown on the right-hand side. Snapshot (A) was taken during the exponential growth phase, and snapshot (B) during the CA phase, after the downward chirp. In each snapshot, a horizontal dashed line indicates the instantaneous mode frequency $\omega_{n=3}$, and white curves represent the shear Alfvén continua $\omega_{\rm A}(r)$.

Clearly, the mode frequency tends to be larger for larger values of Γ. This trend can be attributed to the increasing effect that compressibility has on the bulk plasma response when Γ is increased, because it is clearly correlated with the increasing up-shift of the shear Alfvén continua $\omega_{\rm A}$, which are plotted as white curves in each of the snapshots on the right-hand side of Fig. 14.

7.3. Multi-n simulations with FLR and different values of Γ

Finally, let us consider multi-n simulations performed with fast ion FLR (gyroaveraging) for three values of the specific heat ratio, $\Gamma = 1$, $5/3$ and 3. Figure 15 shows the evolution of the amplitudes $A_n(t)$ of the $n = 1$–4 modes, as well as their effect on the fast ion beta profile $\beta_{\rm h,gc}(r_{\rm lfs})$. Note that $\beta_{\rm h,gc}(r_{\rm lfs})$ plotted in Fig. 15(d) is the guiding center (GC) profile; i.e., it is computed without gyroaveraging. The $n = 2$ and $n = 4$ harmonics are strongly affected by MHD nonlinearities associated with the $n = 1$ and $n = 3$ harmonics. In the following, we discuss only the $n = 1$ and $n = 3$ modes, whose evolution is dominated by resonant drive from fast ions.

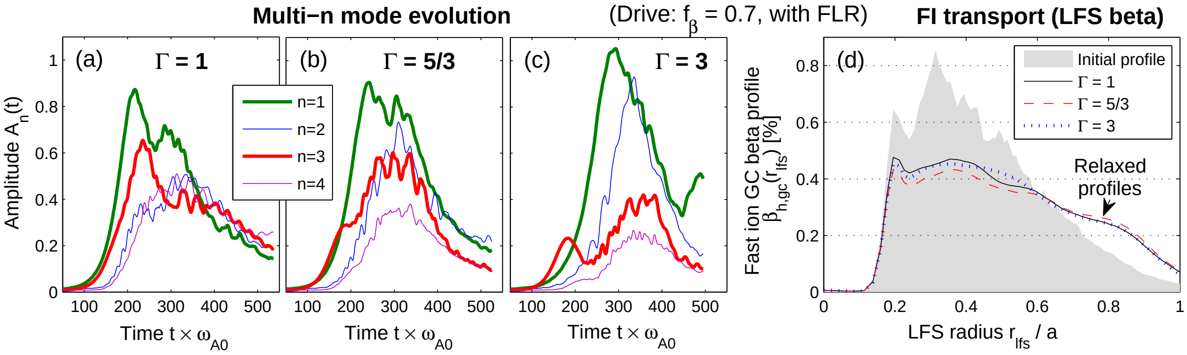

Figure 15. Effect of the specific heat ratio Γ on the evolution of resonant instabilities and resulting fast ion transport in multi-n simulations with $f_\beta = 0.7$ and fast ion FLR (gyroaveraging). (a)–(c): Evolution of the amplitudes $A_n(t)$ for $n = 1$, 2, 3 and 4 for three values of $\Gamma = 1$, 5/3 and 3. (d): Comparison between initial (shaded) and relaxed fast ion guiding center (GC) beta profiles $\beta_{\rm h,gc}(r_{\rm lfs})$ in each case.

In all three cases, $\Gamma = 1$, 5/3 and 3, the $n = 1$ mode reaches the largest amplitude because it is least affected by gyroaveraging (as discussed in Section 6 above). Interestingly, the growth rate $\gamma_{n=1}$ of the $n = 1$ mode decreases with increasing Γ, while the saturation amplitude $A_{n=1}(t_{\rm sat})$ increases: $\gamma_{n=1} = 0.035$, 0.031, 0.028, and $A_{n=1}(t_{\rm sat}) = 0.87$, 0.91, 1.05 for $\Gamma = 1$, 5/3, 3, respectively. This is different from the $n = 3$ mode, whose linear growth rate is insensitive to Γ in the present case, while its saturation amplitude decreases with increasing Γ (see Section 7.1 and Fig. 12 above). Indeed, for $\Gamma = 5/3$ and $\Gamma = 3$ in Figs. 15(b) and 15(c), the $n = 3$ mode grows grows faster than $n = 1$. However, $n = 3$ saturates at a relatively low amplitude and is eventually overtaken by $n = 1$.

Clearly, the variation of Γ can have different and even opposite effects on modes with different toroidal mode numbers n. It is reasonable to assume that the trends seen in Fig. 12 are not generic but case-dependent. In particular, we conjecture that the differences observed can be attributed to Γ shifting the continuous spectra with respect to the resonant frequencies. If so, different behavior can be expected in different MHD equilibria (safety factor, pressure and density profiles) and for different fast ion distributions (radial profile, pitch angle distribution, birth energy).

Evidence that supports this conjecture can be found in Fig. 14 above, where we have seen that the $n = 3$ mode frequency $\omega_{n=3}$ increases with increasing Γ, as the mode effectively follows the lower accumulation point of the toroidicity-induced gap (as discussed in Section 7.2 above). This means that the $n = 3$ mode is driven by different groups of resonant particles for different values of Γ.

Details of the evolution of the dominant $n = 1$ mode in multi-n simulations with fast ion FLR are summarized in Fig. 16. In snapshot (A), which was taken at $t = 130$ during the exponential growth phase, one can see in Fig. 16(b) that the frequency of the linear $n = 1$ mode increases with increasing Γ; namely, $\omega_{n=1} = 0.236$, 0.243, 0.258. However, this increase in $\omega_{n=1}$ is smaller than the Γ-induced up-shift of the continuum.

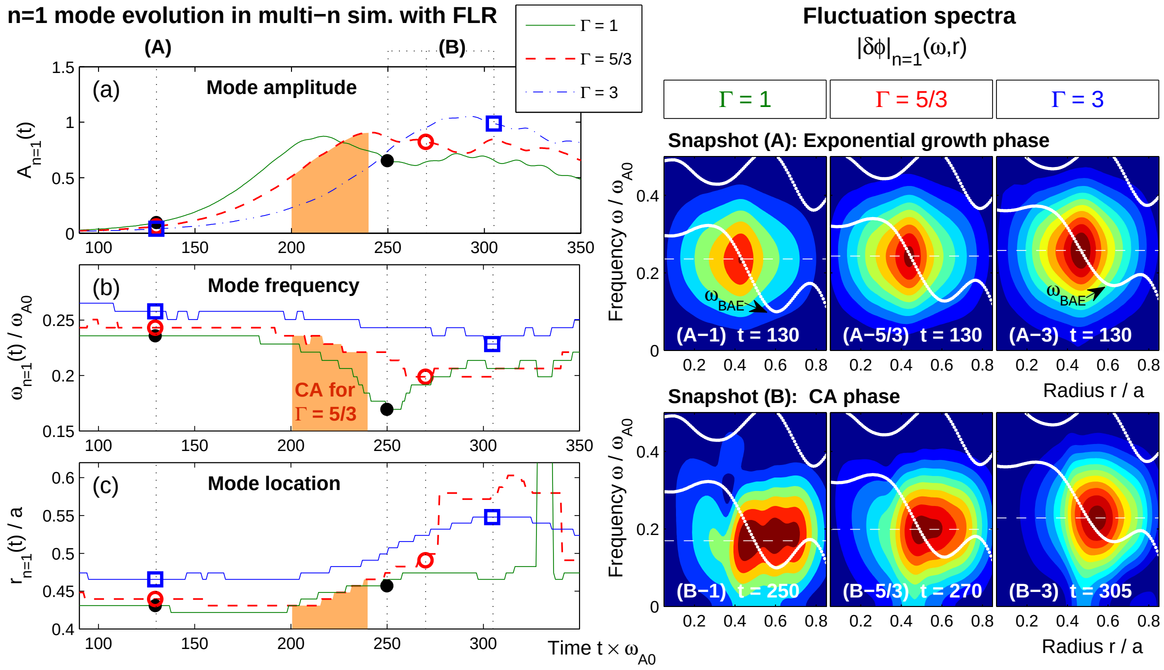

Figure 16. Effect of the specific heat ratio Γ on the convective amplification (CA) and chirping of the $n = 1$ mode in multi-n simulations that include fast ion FLR and are performed with $f_\beta = 0.7$. (cf. Fig. 15). Arranged as Fig. 14. Here, snapshot (A) was taken during the exponential growth phase, and snapshot (B) at the time where the mode frequency reaches its lowest value.

For instance, the accumulation point of the compressibility induced gap just next to the $n = 1$ mode is located at $\omega_{\rm BAE} = 0.10,\ 0.13,\ 0.17$ for $\Gamma = 1,\ 5/3,\ 3$, respectively. Consequently, the fluctuation spectrum of the $n = 1$ mode in snapshot (A-3) is closer to the accumulation point of the compressibility-induced gap than in snapshot (A-1). Nevertheless, the linear $n = 1$ mode manages to remain on the shear Alfvén continuum by shifting radially outward with increasing Γ, as can be seen from the values of $r_{n=1}$ at snapshot (A) in Fig. 16(c); namely, $r_{n=1} = 0.43,\ 0.44,\ 0.47$.

The different structure of the continua around the linear $n = 1$ eigenmode for different values of Γ suggests that, in order to propagate radially outward during the convective amplification (CA) phase, the mode frequency requires much less adjustment in the $\Gamma = 3$ case than for $\Gamma = 1$. Indeed, Fig. 16(b) shows that, between snapshots (A) and (B), the down-chirp in the $\Gamma = 3$ case, where $\omega_{n=1}(\mathrm{A}) = 0.26 \rightarrow \omega_{n=1}(\mathrm{B}) = 0.23$, is significantly smaller than in the $\Gamma = 1$ case, where $\omega_{n=1}(\mathrm{A}) = 0.24 \rightarrow \omega_{n=1}(\mathrm{B}) = 0.17$. It seems that a reduction of chirping is beneficial for CA in the present scenario, which explains that, in Fig. 16(a), the peak amplitude of the $n = 1$ mode increases with increasing Γ. The interconnection between chirping and CA remains to be understood.

Finally, let us emphasize once more that the trends described in this section are most likely case-specific. As mentioned at the beginning of Section 7, the Γ-dependence of the mode dynamics must be expected to vary from case to case, depending on the equilibrium profiles and fast ion distribution.

8. Summary and conclusion

In this paper, we have studied the sensitivity of the growth and nonlinear evolution of fast-ion-driven modes with respect to several simulation parameters; namely, the choice of particle boundary conditions for fast ions, the values of diffusion coefficients, the use of gyroaveraging over fast ion Larmor radii, and the degree of compressibility of the bulk plasma. In order to characterize the effect on the nonlinear dynamics, we have paid particular attention to frequency chirping (which may be quasi-linear or nonlinear [34, 35]), convective amplification (CA) [25], and fast ion transport. In particular, we examined the threshold for the transition from low- to large-amplitude mode activity (and, thus, weak to strong transport) through the onset of CA by varying the strength of the resonant drive via the parameter f_β defined in Eq. (4).

The scope of this work is limited to long-wavelength modes ($n \gtrsim 1$) with frequencies in the toroidicity-induced Alfvén gap or in the surrounding shear Alfvén continua. The conclusions that can be drawn on the basis of the results presented here are strictly valid only for the short-time response of the plasma, in the presence of relatively strong resonant drive from fast ions; namely, near the threshold for the onset of CA. Hence, it is possible that the long-time behavior of the system in the presence of weakly driven modes will exhibit a different degree of sensitivity with respect to the parameters examined here. However, the sensitivity of long-time simulations will be harder to assess due to the larger computational expenses. We anticipate that the results of the present sensitivity study give us a reasonable starting point for the choice of parameters to be used in self-consistent long-time simulations of fast ion dynamics in beam-driven tokamak plasmas, including wave-particle interactions, sources, sinks and collisions.

Below is a summary of the main results obtained in each section and the conclusions that we have drawn. Implications for nonlinear benchmark studies and the relevance of advances made with respect to numerical stability are also discussed.

8.1. Summary of results from parameter scans and implications for long-time simulations

(i) *Section 4: Loss boundary for fast ions.* Simulations were performed with

  (a) artificial fast ion losses at the plasma boundary (last closed flux surface), and
  (b) a realistic fast ion loss boundary at the wall.

Due to large magnetic drifts, the choice of boundary condition was found to have a significant effect on the form of the fast ion distribution. The effect on the growth and nonlinear dynamics of the core-localized fast-ion-driven modes studied here was small in the present short-time simulations (< 1 ms). However, we anticipate that there may be a significant cumulative effect in long-time simulations with continuous low-amplitude fluctuations; in particular, when there are modes that are driven by gradients in the outer part of the plasma, where the loss boundary effect is strong. Therefore, the use of a realistic loss boundary is preferred. It is easy to implement a realistically-shaped wall in a full-f PIC code, where its only disadvantage is an increased computational expense due to the larger size of the spatial simulation domain needed to include the vacuum region.

(ii) *Section 5: Diffusion coefficients.* We examined how the normalized resistivity η and viscosity ν affect the dynamics of fast-ion-driven modes with $n = 3$. The thermal diffusivity was set to $\chi = \min\{\eta, \nu\}$. The following summary is for $\eta = \nu = \chi$:

  (a) **Exponential growth and CA threshold:** When the drive is sufficiently strong, so that the mode is near or above the threshold for CA (where $\gamma/\omega \gtrsim 0.05$), diffusion is found to have a negligible effect on the linear growth rate γ when $\eta \lesssim 3 \times 10^{-6}$. A detailed explanation is given in Appendix A. Essentially, these results mean that, below the threshold for CA, the modes are dominated by the competition between resonant drive and damping mechanisms; whereas, near and above the threshold for CA, the resonant drive dominates until the mode saturates. These simulation results are consistent with the theory for CA developed by Zonca *et al.* [25], which predicts that the transition from low- to high-amplitude Alfvénic fluctuations occurs close to the threshold where resonant drive begins to dominate over damping effects. Below that threshold, the modes can still be unstable, but they saturate at low amplitudes and cause only negligible amounts of transport.

  (b) **CA phase and nonlinear saturation:** As the resonant drive is depleted, resistive and viscous damping effects can become more important. For resistivities between $\eta = 10^{-6}$ and 3×10^{-7}, these effects become noticeable already during the CA phase; namely, the thresholds for the onset of CA and the saturation amplitudes were seen to differ by 10–20%. These quantitative differences become smaller when dissipation is further reduced to $\eta = 10^{-7}$. One may speculate that the threshold for CA becomes effectively independent of resistivity when $\eta \lesssim 10^{-7}$.

  (c) **Decay phase:** The $n = 3$ mode tends to decay more slowly for smaller values of η. However, it is difficult to explain the changes in the decay rate of the mode as a direct consequence of varying η, because the mode radius and frequency also evolve differently for different values of η, and so do the resonant structures in phase space.

Based on the above results together with the discussion of thermal ion FLR effects given at the end of Appendix A, our default choice $\eta = \nu = \chi = 10^{-6}$ appears to be a reasonable compromise to simulate the dynamics of modes with toroidal mode numbers $n = 1$–3 in the practically important parameter regime near the threshold for CA. The amount of diffusion is small enough to allow resonant wave-particle interactions to dominate at the scale of the global modes, while properly closing the MHD model through strong dissipation on spatial scales comparable to the thermal ion Larmor radius $\rho_{\rm Li}$. The choice $\eta = 10^{-6}$ is also reasonable from the point of view of computational expenses. Simulations with $\eta \sim 10^{-7}$ require twice as many grid points in both R and Z, and twice as many time steps, which is still prohibitive for the kind of self-consistent long-time simulations that we are preparing for here.

(iii) *Section 6: Finite Larmor radii (FLR) of fast ions.* While linear growth rates and mode structures varied relatively little for the modes studied, the threshold $f_\beta^{\rm crit}$ for the onset of CA of the $n = 3$ mode varied significantly (by 40%) between the simulations performed with FLR and in the zero-Larmor-radius (ZLR) limit. As expected, the effect of fast ion FLR is weaker for modes with longer wavelength; in particular, the evolution of the $n = 1$ mode was similar in the FLR and ZLR simulations. However, the present study was limited to the short-time response, so we cannot exclude the possibility that even the $n = 1$ mode becomes sensitive to FLR effects when one considers meso-time-scale phenomena (1–10 ms), such as intermittent bursts [17]. Thus, we consider fast ion gyroaveraging to be a crucial ingredient in self-consistent long-time simulations, even for $n = 1$ modes.

(iv) *Section 7: Ratio of specific heats and bulk compressibility.* The specific heat ratio Γ controls the effect of compressibility on the bulk plasma response. Between the the extreme limits $\Gamma = 1$ (weak compressibility effect) and $\Gamma = 3$ (strong compressibility effect), the threshold $f_\beta^{\rm crit}$ for CA of the $n = 3$ mode varied by 30%. The effect on the growth, chirping and saturation amplitude varied between modes. However, instead of being a direct consequence of the varying effect of compressibility, we attribute these changes in the mode dynamics to the fact that Γ alters the structure of the shear Alfvén continua in a high-beta tokamak plasma as that considered here. It must be expected that the effect of Γ varies case-by-case, depending on the equilibrium profiles and fast ion distribution. In long-time simulations, one may take advantage of this fact and vary the specific heat ratio between the extreme limits $\Gamma = 1$ and $\Gamma = 3$ in order to asses the robustness of the results (e.g., dominant up- or downward chirping) with respect to changes in the equilibrium profiles and fast ion distribution, without actually having to modify them. Meanwhile, the usual value $\Gamma = 5/3$ seems to be a reasonable starting point.

(v) *Fast ion transport.* The effect of diffusion coefficients, fast ion FLR, and bulk compressibility on the steady state distribution of fast ions will have to be evaluated using long-time simulations as in Refs. [16, 17, 18]. Meanwhile, the results of the present work give us useful insights relevant to avalanche-like transport that occurs on short time scales. We have shown that our parameters have an influence on the threshold for CA of the $n = 3$ mode (Figs. 7, 11 and 13). Since the onset of CA also marks the transition from weak to strong fast ion transport, the choice of simulation parameters may have an influence on the occurrence of abrupt large relaxation events (ALE) in JT-60U and the associated fast ion avalanches, which we are hoping to reproduce with self-consistent long time simulations. Based on the results reported here, we anticipate that the threshold at which an ALE occurs may vary by 10–20% depending on the values of η, ν ($\lesssim 10^{-6}$) and Γ used. Note, however, that this estimate refers to the amount of drive that is present near the

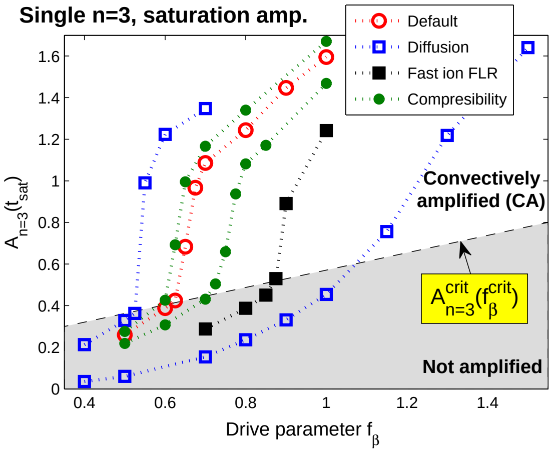

Figure 17. Evidence for a robust linear dependence of the critical amplitude $A^{\rm crit}_{n=3}$ on the critical value of the drive parameter $f^{\rm crit}_\beta$ for the transition from weak to strong $n = 3$ mode activity. This diagram summarizes the results of f_β-scans from Figs. 7(d), 11(c) and 13(d). The function $A^{\rm crit}_{n=3}(f^{\rm crit}_\beta)$ given by Eq. (20) is shown as a dashed line.

resonances of the relevant modes. The sensitivity of the velocity-integrated fast ion beta profile $\beta_{\rm h}(r)$ can be expected to be lower than 10%.

(vi) *Critical amplitude for CA.* Concerning the conditions for the onset of CA, an interesting observation can be made when the results of all f_β-scans are combined in one diagram as shown in Fig. 17. The $n = 3$ mode in the scenario studied is subject to CA when the drive parameter f_β defined in Eq. (4) exceeds a critical value $f^{\rm crit}_\beta = f^{\rm crit}_\beta(\eta, \rho_{\rm Lh}, \Gamma)$. This critical value of the drive parameter depends on the individual values of all the parameters that we have varied: resistivity η (Fig. 7), fast ion Larmor radius $\rho_{\rm Lh}$ (Fig. 11), and specific heat ratio Γ (Fig. 13). The remarkable feature to be seen in the combined Fig. 17 is that the critical saturation amplitude $A^{\rm crit}_{n=3}$ at which the transition occurs is simply a linear function of $f^{\rm crit}_\beta$,

$$A^{\rm crit}_{n=3} \approx c_1 + c_2 f^{\rm crit}_\beta, \quad \text{for} \quad 0.4 \lesssim f^{\rm crit}_\beta(\eta, \rho_{\rm Lh}, \Gamma) \lesssim 1. \tag{20}$$

This function is plotted as a dashed line in Fig. 17. The coefficients $c_1 = 0.3$ and $c_2 = (0.8 - 0.3)/(1.55 - 0.35)$, and thus the critical amplitude $A^{\rm crit}_{n=3}$ appear to be independent of the individual values of η, $\rho_{\rm Lh}$ and Γ. There is evidence that CA plays an important role in the triggering of ALEs [8, 9], so it may be useful to study the generality of Eq. (20). This may reveal interesting nonlinear physics that are relevant to such relaxation phenomena, and it may be useful for the construction of reduced models for fast ion confinement in the presence of strong MHD activity.

8.2. Implications for nonlinear benchmark studies

For the present sensitivity study, we have made extensive use of the transition from weak to strong mode activity via the onset of convective amplification (CA). This may also be a useful strategy for cross-code benchmark activities concerned with nonlinear dynamics. The reason is that different codes use different models, so it is not necessarily meaningful to use precisely the same parameter values in all codes that participate in a nonlinear benchmark study. Instead, it may be more meaningful to allow for a certain leeway in the choice of parameter values and to use this freedom to make sure that all codes are simulating the same dynamic regime. For instance, one may compare results obtained in the regime just below and just above the threshold for CA, while allowing that the critical value of the fast ion pressure gradient — here, measured by the drive parameter f_β defined in Eq. (4) — may be somewhat different for different codes. After one has shown that the codes are all in the same dynamic regime (e.g., below or above the CA threshold), one may begin with more detailed comparisons; e.g., by examining nonlinear phase space structures using Hamiltonian mapping techniques [36].

8.3. Advances made in numerical stability

In addition to the CA of individual toroidal harmonics (here $n = 3$), nonlinear interactions between modes with different values of n are also likely to play an important role for the occurrence of intermittent relaxations, such as ALEs. These interactions may include both MHD nonlinearities (forward and inverse cascade of fluctuation energy) and wave-particle nonlinearities (linear and nonlinear resonance overlaps). In order to simulate these processes, we had to overcome problems of numerical stability. As reported in Figs. 14 and 16 of Ref. [9], our previous attempts to perform multi-n simulations of strongly driven Alfvén modes (i.e., above the threshold for CA) in the present high-beta JT-60U scenario were only partially successful. Due to nonlinear instabilities, these simulations terminated soon after nonlinear saturation; i.e., long before a fully relaxed state was reached. Recently, we have resolved these problems as described in Appendix C by (I) enhancing the digital filtering of bulk pressure and density, and (II) smoothing the plasma boundary. With this, the multi-n simulations reported in this work (Figs. 2, 4, 15 and 16) ran smoothly without obvious problems.

Together with the results of the sensitivity study reported in this paper, these numerical advances prepare MEGA for comprehensive long-time simulations of N-NB-driven high-beta JT-60U and JT-60SA scenarios, which include self-consistent wave-particle interactions, sources and collisions, and can cover a wide range of time scales, from Alfvénic oscillations and fast ion motion ($\lesssim$ 10 μs), via intermittent bursts of Alfvén mode activity and avalanches ($\sim$ 0.1–10 ms), to collisional slow-down ($\gtrsim$ 100 ms).

Acknowledgments

One of the authors (A.B.) would like to thank M. Yagi for helpful discussions and continuous support of this research. This work has been partially supported by Grant-in-Aid for Scientific Research from the Japan Society for the Promotion of Science (JSPS), Grant No. 25820443. The simulations were carried out using the supercomputer system HELIOS at IFERC, Aomori, Japan, under the Broader Approach collaboration between

Euratom and Japan, implemented by Fusion for Energy and QST.

Appendix A. Resistive diffusion and spatial grid

An important decay mechanism for Alfvénic modes in the resistive MHD model used in MEGA is continuum damping. Continuum damping begins with phase mixing, which transfers energy from longer to shorter radial scale lengths at a rate $\gamma_{\rm mix}$, and ends with the dissipation of the energy contained in the small-scale structures. Without resistivity (and viscosity), the small-scale structures would be dissipated numerically due to the finite grid size. They may also cause numerical instabilities. With sufficiently large resistivity and a sufficiently fine grid, these structures can be dissipated in a more physical manner and converted to heat in the equation of state for the thermal bulk pressure $p_{\rm b}$ [Eq. (10)]. In this appendix section, we discuss the resistive diffusion process and numerical requirements that must be satisfied to simulate it. This discussion also applies to the effect of viscosity and thermal diffusivity when $\eta = \nu = \chi$, since the respective diffusion equations have the same form.

Combining Eqs. (7), (8) and (9), the evolution of the magnetic field is given by

$$\underbrace{\frac{\partial \boldsymbol{B}}{\partial t}}_{\rm (i)} = \underbrace{\boldsymbol{\nabla}\times(\delta\boldsymbol{u}\times\boldsymbol{B})}_{\rm (ii)} + \underbrace{\frac{\eta}{\mu_0}\boldsymbol{\nabla}\times(\boldsymbol{\nabla}\times\boldsymbol{B})}_{\rm (iii)}. \tag{A.1}$$

Together with the momentum equation for $\delta\boldsymbol{u}$ [Eq. (6)], the balance between terms (i) and (ii) in Eq. (A.1) yields an Alfvén wave equation, which determines the real component of the frequency, $\mathrm{Re}\{i\partial/\partial t\} \leftrightarrow \omega$. Meanwhile, the balance between terms (i) and (iii) in Eq. (A.1) yields a magnetic diffusion equation, which contributes to the imaginary component of the frequency, $\mathrm{Im}\{i\partial/\partial t\} \leftrightarrow \gamma$, where $\gamma > 0$ represents growth and $\gamma < 0$ represents decay. The magnitude of the resistive decay rate for structures with wavelength λ is then given by

$$|\gamma_\eta| \sim \frac{\eta}{\mu_0}\left(\frac{2\pi}{\lambda}\right)^2 \quad \rightarrow \quad \left|\frac{\gamma_\eta}{\omega_{\rm A0}}\right| \sim \left(\frac{2\pi R_0}{\lambda}\right)^2 \hat{\eta} \approx \frac{40\times\hat{\eta}}{(\lambda/R_0)^2}; \tag{A.2}$$

where the normalized resistivity $\hat{\eta}$ in Eq. (A.2) is defined as

$$\hat{\eta} \equiv \frac{\eta}{\mu_0 v_{\rm A0} R_0} = \frac{a}{R_0}\frac{1}{S_{\rm p}} \tag{A.3}$$

The quantity $S_{\rm p} = \tau_\eta/\tau_{\rm pA0}$ is the "poloidal Lundquist number" that is widely used in resistive reduced MHD studies and measures the ratio between the resistive diffusion time $\tau_\eta = \mu_0 a^2/\eta$ and the shear Alfvén wave propagation time $\tau_{\rm pA0} = a/v_{\rm A0} = a/(R_0\omega_{\rm A0})$ on the length scale a. Thus, $\hat{\eta}$ in Eq. (A.3) may be interpreted as the ratio of Alfvén time to resistive time on the length scale of the major radius R_0.

Using the plasma parameter values summarized in Table A1, we can estimate the value of the normalized resistivity $\hat{\eta}$ in the core of the beam-driven JT-60U plasma studied in this work to be around $\hat{\eta} \approx (1...5)\times 10^{-9}$. The corresponding poloidal

R_0 [m]	a [m]	$a_{\rm lfs}$ [m]	B_0 [T]	$T_{\rm e0}$ [keV]	$n_{\rm e0}$ [$10^{20}{\rm m}^{-3}$]	$n_{\rm i0}$ [$10^{20}{\rm m}^{-3}$]	$Z_{\rm eff}$
3.395	0.953	0.66	1.2	2.1	0.22	0.17	1.3...2.6

Table A1. Plasma parameters for the JT-60U scenario studied in this paper, which is based on shot E039672 at 4 seconds. Here, R_0 is the major radius of the magnetic axis, $a \equiv \sqrt{V_a/(2\pi^2 R_0)}$ is the characteristic minor radius of the plasma defined in terms of its volume V_a, and $a_{\rm lfs}$ is the minor radius on the low-field side (outer mid-plane). The magnetic field strength B_0, electron temperature $T_{\rm e0}$ and densities $n_{\rm e0}$ and $n_{\rm i0}$ are given at the magnetic axis. For this shot, the reference value for the effective charge number is $Z_{\rm eff} = 2.1$. However, this estimate has some degree of uncertainty. Moreover, there is presumably also a strong radial dependence. Since the resistivity scales as $\eta \propto Z_{\rm eff}^2$ (cf. Eq. (A.6)), it is rather sensitive to the value of $Z_{\rm eff}$. Thus, we compute η in Eq. (A.7) for the range $Z_{\rm eff} = 1.3...2.6 \approx (1...2) \times n_{\rm e}/n_{\rm i}$.

Lundquist number is $S_{\rm p} \approx (2...1) \times 10^8$. The details of this calculation are as follows:

$$v_{\rm A0} = \frac{B_0}{\sqrt{\mu_0 m_{\rm i} n_{\rm i}}} = 4.5 \times 10^6\,{\rm m/s}, \tag{A.4}$$

$$\begin{aligned}\ln\Lambda_{\rm e} &= \ln\left[2\pi n_{\rm e}\left(\frac{\epsilon_0 T_{\rm e}}{n_{\rm e}e^2}\right)^{3/2}\right] = \ln\left[\frac{2\pi}{10^{10}}\left(\frac{\epsilon_0}{e}\right)^{3/2}\frac{(T_{\rm e}[{\rm eV}])^{3/2}}{(n_{\rm e}[10^{20}{\rm m}^{-3}])^{1/2}}\right] \\ &= \ln\left[256 \times \frac{2100^{3/2}}{0.22^{1/2}}\right] = 17.8,\end{aligned} \tag{A.5}$$

$$\begin{aligned}\nu_{\rm ei\|} &= \frac{Z_{\rm eff}^2 e^4 n_{\rm i}\ln\Lambda_{\rm e}}{4\pi\epsilon_0^2\sqrt{m_{\rm e}}T_{\rm e}^{3/2}} = \frac{e^{5/2}10^{20}}{4\pi\epsilon_0^2\sqrt{m_{\rm e}}}\frac{Z_{\rm eff}^2\ln\Lambda_{\rm e}n_{\rm i}[10^{20}{\rm m}^{-3}]}{(T_{\rm e}[{\rm eV}])^{3/2}} \\ &= 1.1 \times 10^9 \times \frac{(1.3...2.6)^2 \times 17.8 \times 0.17}{2100^{3/2}} = (0.6...2.3) \times 10^5\,{\rm s}^{-1},\end{aligned} \tag{A.6}$$

$$\begin{aligned}\eta &= \frac{1}{4}\frac{m_{\rm e}}{n_{\rm e}e^2}\nu_{\rm ei\|} = \nu_{\rm ei\|} = \frac{m_{\rm e}}{4e^2 10^{15}}\frac{\nu_{\rm ei\|}[10^5{\rm s}^{-1}]}{n_{\rm e}[10^{20}{\rm m}^{-3}]} \\ &= 8.9 \times 10^{-9} \times \frac{(0.6...2.3)}{0.22} = (2.4...9.3) \times 10^{-8}\,\Omega{\rm m},\end{aligned} \tag{A.7}$$

$$\hat\eta = \frac{\eta}{\mu_0 v_{\rm A0} R_0} = \frac{\eta[\Omega{\rm m}]}{19.2} = (1.3...4.8) \times 10^{-9}; \tag{A.8}$$

where $m_{\rm i}$ is the mass of a deuteron.

The global structure of the long-wavelength modes studied in this paper is characterized by $\lambda/R_0 \gtrsim 0.03$ in the minor radial direction (and much larger along ϑ and ζ). Consequently, Eq. (A.2) implies that resistivity has a significant effect on the evolution of these modes only when their growth rates γ satisfy

$$\left|\frac{\gamma}{\omega_{\rm A0}}\right| \lesssim \left|\frac{\gamma_\eta}{\omega_{\rm A0}}\right| \lesssim 4 \times 10^4 \times \hat\eta, \tag{A.9}$$

For the relatively large resistivities around $\hat\eta \sim 10^{-6}$ used in typical MHD and hybrid simulations of Alfvén modes, the resulting value $\gamma_\eta/\omega_{\rm A0} \approx 0.04$ is comparable to the linear growth rates $\gamma_{\rm lin}/\omega_{\rm A0}$ that are achieved below the threshold for convective amplification (CA). Thus, for convectively amplified modes simulated with $\hat{\eta} \lesssim 10^{-6}$, resistivity can be expected to play a role mainly in the nonlinear phase. This is consistent with the results in Figs. 5–8, where we saw that the linear growth rates were independent of resistivity as long as $\hat{\eta} \lesssim 3 \times 10^{-6}$.

After the resonant drive is exhausted, it can no longer compensate the effect of radial phase mixing that occurs in those regions where the fluctuation spectrum $|\delta\phi|_n(\omega, r)$ of the mode intersects some part of the continuous spectrum. Note that phase mixing only changes the mode structure and does not directly contribute to the decay of the mode energy that can be seen in the time traces of the amplitude $A_n(t) = W_n^{1/2}(\mathrm{t})$, which we computed using Eq. (18). The decay of $A_n(t)$ is caused by resistivity and viscosity terms that diffuse the gradients of the mode structure and eventually transfer that energy to the background profiles ($n = 0$). Phase mixing tends to steepen those gradients and this, in turn, enhances the effect of diffusion. In this way, phase mixing contributes to the decay of the mode, and this contribution is known as "continuum damping".

The strength of diffusion in the simulations must be kept sufficiently strong to prevent phase mixing from generating structures with radial scale lengths that are not adequately resolved by the spatial grid used. In our simulations, the spatial size L of the simulated domain and the number N of grid points along each dimension of the right-handed cylindrical coordinate system (R, φ, Z) are

$$\begin{bmatrix} L_R \\ L_\varphi \\ L_Z \end{bmatrix} \approx \begin{bmatrix} 2.26\,\mathrm{m} \\ 2\pi/n_{\mathrm{min}} \\ 3.16\,\mathrm{m} \end{bmatrix}, \qquad \begin{bmatrix} N_R \\ N_\varphi \\ N_Z \end{bmatrix} \approx \begin{bmatrix} 384 \\ 32 \times n_{\mathrm{max}} \\ 352 \end{bmatrix}. \tag{A.10}$$

Thus, the size of the spatial cells in the poloidal plane (R, Z) is

$$\Delta R/R_0 \approx 1.7 \times 10^{-3}, \qquad \Delta Z/R_0 \approx 2.6 \times 10^{-3}, \tag{A.11}$$

which allows to resolve structures with wavelengths λ satisfying $\lambda/R_0 \gtrsim 8\Delta Z/R_0 \approx 3 \times 10^{-3}$. For the default value of $\hat{\eta} = 10^{-6}$, structures of that size are suppressed by resistive dissipation if

$$\left|\frac{\gamma_{\mathrm{mix}}}{\omega_{\mathrm{A0}}}\right| \ll \left|\frac{\gamma_\eta}{\omega_{\mathrm{A0}}}\right| \sim \frac{40 \times \hat{\eta}}{(8\Delta Z/R_0)^2} \approx 0.1 \qquad \text{for} \quad \hat{\eta} = 10^{-6}. \tag{A.12}$$

Equation (A.12) means that resistive dissipation is effective only if the phase mixing rate $|\gamma_{\mathrm{mix}}/\omega_{\mathrm{A0}}|$ is significantly slower than the resistive decay rate $|\gamma_\eta/\omega_{\mathrm{A0}}| \sim 10^{-1}$ on the scale of the grid $(\Delta R, \Delta Z)$. We have seen in Fig. 8 that, after nonlinear saturation, it takes about 100 Alfvén times for the amplitudes of the modes in our simulations to decay by a factor $\exp(1) \approx 3$, so the overall damping rate is of the order $|\gamma/\omega_{\mathrm{A0}}| \sim \mathcal{O}(10^{-2})$. This can be interpreted as an estimate for the upper limit of the phase mixing rate γ_{mix} because we do not observe the formation of any "singular" radial structures when the modes decay in our simulations. This upper limit of 10^{-1} for γ_{mix} is one order of magnitude smaller than γ_η in Eq. (A.12) for $\hat{\eta} = 10^{-6}$, so that we may assume that radial phase mixing in our simulations terminates in resistive heating, and that no significant amount of energy is dissipated by the spatial grid.‡

---

‡ In MHD stable low-beta equilibria, this can be verified by measuring the quality of energy

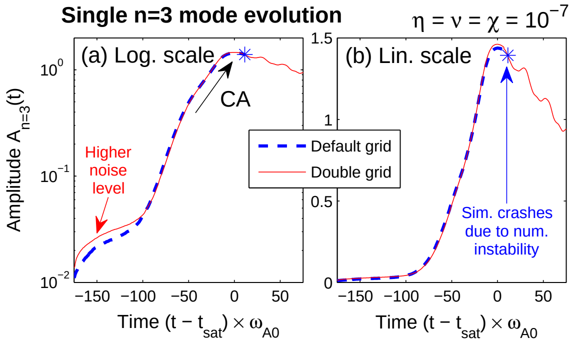

Figure A1. Simulation results illustrating how the numerical stability of MEGA depends on the proper choice for the spatial grid and resistive diffusion. A single-n simulation for the fast-ion-driven $n = 3$ mode is performed with drive parameter $f_\beta = 0.7$ and weak diffusion, $\hat{\eta} = \hat{\nu} = \hat{\chi} = 10^{-7}$. The evolution of the mode amplitude $A_{n=3}(t)$ is shown on a logarithmic (a) and linear scale (b).

To test this assumption, we demonstrate in Fig. A1 that our default spatial grid specified in Eq. (A.10) does not suffice any more when the diffusion coefficients are reduced by one order of magnitude to $\hat{\eta} = \hat{\nu} = \hat{\chi} = 10^{-7}$. Figure A1 shows the evolution of the $n = 3$ mode amplitude for two cases: once we used the default number of grid points $N_R \times N_Z = 384 \times 352$ (dashed) and another time the number of grid points was doubled to $N_R \times N_Z = 768 \times 704$ (solid), with a corresponding reduction of the time step by a factor 2. One can see that the results of the two simulations agree well as long as the resonant drive is dominant and strong; namely, during the exponential growth and convective amplification (CA) phases, until the mode saturates at $t = t_{\rm sat}$.[𝒮] However, shortly after saturation, the simulation with the default grid terminates prematurely due to a numerical instability. This indicates that the decaying mode transfers a significant amount of energy to structures with wavelength that cannot be resolved with the default grid. Such numerical instabilities serve as a safety mechanism that tells us to either increase the spatial resolution or to raise the values of the diffusion coefficients.

Our goal is to carry out self-consistent long-time simulations (up to ~ 100 ms), which is presently feasible only with a few 100 grid points in each direction. With the choice $\hat{\eta} = 10^{-6}$ for the resistivity as well as for the other diffusion coefficients, $\hat{\nu}$ and $\hat{\chi}$, we can ensure that this spatial resolution is sufficient.

In addition to this practical constraint, there is also a physical justification for using a resistivity that is much larger than the value $\hat{\eta} \sim 10^{-9}$ that we have estimated above for JT-60U on the basis of collisions only. Namely, $\hat{\eta} = 10^{-6}$ can be interpreted

---

conservation in MEGA. However, in the present high-beta scenario, toroidal Fourier filters are required in order to suppress resistive MHD ballooning instabilities with $n \gtrsim 4$, so that energy conservation is broken by default. Thus, not all energy is converted to heat; some of it is lost through the filters.

[𝒮] The only notable difference lies in the noise level, whose effect can be seen at the beginning of the simulations, around $(t - t_{\rm peak})/\omega_{\rm A0} \lesssim -100$ in Fig. A1(a). Because the number of simulation particles is kept constant ($N_{\rm p} = 28 \times 10^6$), the number of particles per cell is reduced by a factor 4 when N_R and N_Z are doubled. This causes roughly a doubling of the noise level in the fluctuation amplitude $A_{n=3}$.

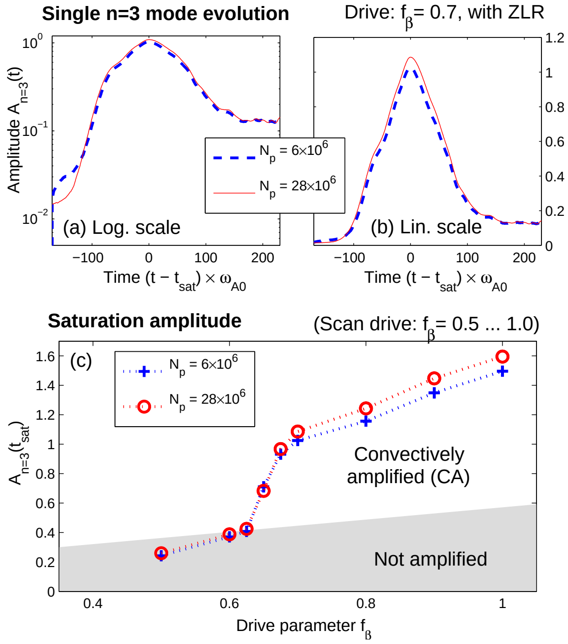

Figure A2. Numerical convergence with respect to the number of simulation particles N_p in a single-n simulation for $n = 3$ in the ZLR limit. Results obtained with $N_\mathrm{p} = 8 \times 10^6$ (dashed) and $N_\mathrm{p} = 28 \times 10^6$ (solid) are compared. (a) and (b): Evolution of the mode amplitude $A_{n=3}(t)$ on a logarithmic and linear scale for the default value of the drive parameter, $f_\beta = 0.7$. (c): Saturation amplitudes $A_{n=3}(t_\mathrm{sat})$ plotted as a function of the drive parameter varied around the threshold for CA, in the range $0.5 \leq f_\beta < 1.0$.

as an “anomalously increased effective resistivity” that mimics kinetic damping effects of the bulk plasma, such as Landau damping and radiative damping, which are not otherwise captured by the MHD model. By letting $\hat{\eta} = \hat{\nu} = 10^{-6}$, we effectively suppress components of the wave packet that oscillate at frequencies $\omega/\omega_\mathrm{A0} \sim 0.25$ (as in Fig. 2) and have wavelengths comparable to the thermal ion Larmor radii ρ_Li. This can be seen by letting $\lambda = \rho_\mathrm{Li} \sim \sqrt{T_\mathrm{e}/m_\mathrm{i}}/\omega_\mathrm{Li} \approx 6 \times 10^{-3}$ m in Eq. (A.2), which gives

$$\left|\frac{\gamma_\eta}{\omega}\right| \sim \frac{40 \times \hat{\eta}}{(\rho_\mathrm{Li}/R_0)^2} \frac{\omega_\mathrm{A0}}{\omega} \sim 4 \qquad \text{on length scales} \quad \lambda \sim \rho_\mathrm{Li}. \tag{A.13}$$

Clearly, it is not physically meaningful to reduce the resistivity $\hat{\eta}$ below 10^{-7}. The same counts for the viscosity $\hat{\nu}$ and thermal diffusivity $\hat{\chi}$. The anomalously increased effective diffusion coefficients are important for the practical realization of MHD closure in a physically meaningful way.

This also means that extended hybrid simulations that account for kinetic thermal ion (KTI) effects would have to be run with $\hat{\eta} \sim \hat{\nu} < 10^{-7}$ in order to ensure that resistive dissipation does not dominate over thermal ion FLR effects such as radiative damping. This would require $N \gtrsim 10^3$ grid points in each dimension (at least in the poloidal plane) and correspondingly small time steps. With presently available computational resources, this may be feasible for short-time simulations (< 1 ms). However, for the long-time simulations that we have in mind here, thermal ion FLR effects are still beyond reach.

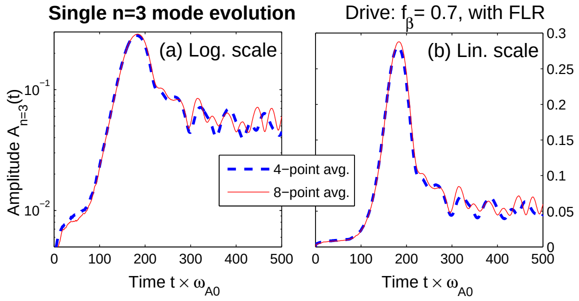

Figure B1. Numerical convergence with respect to the number of satellite particles $N_{\rm gyro}$ used for gyroaveraging. The evolution of the amplitude $A_{n=3}(t)$ of the $n = 3$ mode is shown on a logarithmic (a) and linear scale (b) for $f_\beta = 0.7$. Results obtained with the default value $N_{\rm gyro} = 4$ (dashed) and the increased value $N_{\rm gyro} = 8$ (solid) are compared.

At best, kinetic compression of drift-kinetic thermal ions may be captured, as proposed in Ref. [21].

Appendix B. Numerical convergence with the number of particles

The simulation results presented in this paper were obtained with a relatively large number of simulation particles, $N_{\rm p} = 28 \times 10^6$, because the same simulations were also used to study resonance conditions and phase space structures [28, 34, 35]. However, as far as the evolution of the fast-ion-driven modes is concerned, very similar results can be obtained with a significantly lower particle number of $N_{\rm p} = 8 \times 10^6$, as we have used in Ref. [9]. This is demonstrated in Fig. A2 for the $n = 3$ mode. One can see in panels (a) and (b) that the time traces of the mode amplitude $A_{n=3}(t)$ during its growth, convective amplification (CA), saturation and decay phase are very similar in both cases. In addition, Fig. A2(c) shows that the difference between the absolute values of the peak amplitudes $A_{n=3}(t_{\rm peak})$ obtained with $N_{\rm p} = 8 \times 10^6$ and 28×10^6 is less than 7%. Most remarkably, the sensitive threshold for the onset of CA, here at $f_\beta^{\rm crit} = 0.625$, is exactly reproduced.

In simulations that include the effect of fast ion FLR, the number of simulation particles was effectively increased by a factor 4 due to the use of $N_{\rm gyro} = 4$ satellite particles as was illustrated in Fig. 1. In Fig. B1, we demonstrate that the results obtained with $N_{\rm gyro} = 4$ are similar to those obtained in a simulation using $N_{\rm gyro} = 8$. The noise level in the latter case was reduced, but at the expense of nearly doubling the computation time. We conclude that $N_{\rm gyro} = 4$ is sufficient to simulate the effect of gyroaveraging associated with fast ion FLR in the present scenario with low-n modes.

Appendix C. Digital filter and boundary smoothing

MEGA offers the possibility to apply a digital filter (smoother+compensator, see p. 438 of Ref. [37]) throughout the simulation domain; here, at intervals of $\Delta t_{\rm filt} = 0.23$ Alfvén times (200 MHD time steps). The primary purpose is to reduce the effects of noise introduced by the PIC method used to compute the fast ion current density $\delta\boldsymbol{j}_{\rm h,eff}$ that is substituted into the momentum balance equation, Eq. (6). Of course, this digital filter also contributes to the damping of small-scale structures produced by phase mixing (cf. Appendix A). In order to minimize such numerical damping, the digital filter is usually applied only to the difference between the current signal and the filtered signal from the previous filtering step; e.g., $\boldsymbol{B}(t) - \boldsymbol{B}(t - \Delta t_{\rm filt})$.

The only exceptions are the bulk density and pressure fields, $\rho_{\rm b}$ and $p_{\rm b}$, where the digital filter is applied to the difference between the current signal and the equilibrium field; e.g., $\rho_{\rm b}(t) - \rho_{\rm b}(t = 0)$. While retaining the instantaneous compressible response of the plasma, this method reduces the accumulation of unphysical artifacts that tend to build up in these advected scalar fields during the course of long-time simulations. In the core of the plasma, such artifacts may be caused by the lack of realistic parallel dynamics in the MHD model. In the periphery, artifacts may arise from the zig-zag-shaped plasma boundary in the discretized (R, Z) plane.

It seems that the build-up of such artifacts into singular spikes near the plasma boundary was responsible for the premature termination of multi-n simulations as reported in Figs. 14 and 16 of Ref. [9]. The problem was resolved by enhancing the effect of the digital filter on the scalar fields $\rho_{\rm b}$ and $p_{\rm b}$ as described in the previous paragraph, and by smoothing the plasma boundary as follows.

Originally, the MHD boundary condition applied by multiplying the fluctuating fields with a binary mask that has the value 1 inside the plasma and the value 0 outside. Now, this mask can be smoothened by averaging $N_{\rm smooth}$ times over neighboring grid points. For single-n simulations and in multi-n simulations with moderate drive, $N_{\rm smooth} = 2$ appears to be sufficient. In multi-n simulations with strong drive, $N_{\rm smooth} = 8$ is sometimes required.

Note that these numerical techniques are all optional. They are described here because we apply them in the simulations of high-beta JT-60U scenarios with strong N-NB drive as studied in the present work. Other MEGA simulations may not employ these techniques and may be using other methods that are not mentioned here.

Appendix D. Effect of the toroidal Fourier filter

The filtering of toroidal mode numbers is important for simulating nonlinear dynamics. As was discussed in Section 2 of Ref. [9], the $N_\varphi = 96$ grid points used here in the toroidal direction are sufficient for resolving the dynamics of mode numbers up to $n = 4$. If underresolved harmonics with higher toroidal mode numbers are retained in the MHD fields, they can alter the nonlinear evolution substantially, but in an unphysical way.

Our choice to cut the toroidal mode spectrum off at $n = 4$ is due to the fact that, in the high-beta plasma considered here, resistive MHD ballooning modes with $n \geq 4$ are unstable for $\hat{\eta} = \hat{\nu} = \hat{\chi} = 10^{-6}$ (cf. Fig. 2 in Ref. [9]). As discussed in Appendix A, a lower value of η is not feasible for the long-time simulations that we are preparing for, so a compromise had to be made.

Our tests (not shown here) indicate that higher toroidal harmonics $n \geq 4$ can play an important role as energy sinks when the resonantly driven $n = 1$ and $n = 3$ modes reach high amplitudes. One likely consequence is that the threshold for convective amplification is underestimated in our simulations. However, due to constraints imposed by the physical model (resistive MHD ballooning instabilities) and by the available computational resources (limiting the feasible resolution), these effects cannot yet be fully taken into account in the self-consistent long-time simulations for which we are preparing ourselves here.

References

[1] Y. Kusama, G.J. Kramer, H. Kimura, M. Saigusa, T. Ozeki, K. Tobita, T. Oikawa, K. Shinohara, T. Kondoh, and M. Moriyama *et al.* Characteristics of Alfvén eigenmodes, burst modes and chirping modes in the Alfvén frequency range driven by negative ion based neutral beam injection in JT-60U. *Nucl. Fusion*, 39(11Y):1837, 1999.

[2] K. Shinohara, Y. Kusama, M. Takechi, A. Morioka, M. Ishikawa, N. Oyama, K. Tobita, T. Ozeki, S. Takeji, and S. Moriyama *et al.* Alfvén eigenmodes driven by Alfvénic beam ions in JT-60U. *Nucl. Fusion*, 41(5):603, 2001.

[3] K. Shinohara, M. Takechi, M. Ishikawa, Y. Kusama, K. Tsuzuki, K. Urata, H. Kawashima, K. Tobita, A. Fukuyama, and C.Z. Cheng *et al.* Energetic particle physics in JT-60U and JFT-2M. *Plasma Phys. Control. Fusion*, 46(7):S31, 2004.

[4] M. Ishikawa, M. Takechi, K. Shinohara, Y. Kusama, C.Z. Cheng, G. Matsunaga, Y. Todo, N.N. Gorelenkov, G.J. Kramer, and R. Nazikian *et al.* Energetic ion transport by abrupt large-amplitude events induced by negative-ion-based neutral beam injection in the JT-60U. *Nucl. Fusion*, 45(12):1474, 2005.

[5] L. Chen. Theory of magnetohydrodynamic instabilities excited by energetic particles in tokamaks. *Phys. Plasmas*, 1(5):1519, 1994.

[6] Y. Todo, K. Shinohara, M. Takechi, and M. Ishikawa. Nonlocal energetic particle mode in a JT-60U plasma. *Phys. Plasmas*, 12(1):012503, 2005.

[7] S. Briguglio, G. Fogaccia, G. Vlad, F. Zonca, K. Shinohara, M. Ishikawa, and M. Takechi. Particle simulation of bursting Alfvén modes in jt-60u. *Phys. Plasmas*, 14(5):055904, 2007.

[8] A. Bierwage, K. Shinohara, N. Aiba, and Y. Todo. Role of convective amplification of $n = 1$ energetic particle modes for N-NB ion dynamics in JT-60U. *Nucl. Fusion*, 53(7):073007, 2013.

[9] A. Bierwage, Y. Todo, N. Aiba, and K. Shinohara. Dynamics of low-n shear Alfvén modes driven by energetic N-NB ions in JT-60U. *Nucl. Fusion*, 54(10):104001, 2014.

[10] M.S. Chu, J.M. Greene, L.L. Lao, A.D. Turnbull, and M.S. Chance. A numerical

study of the high-n shear Alfvén spectrum gap and the high-n gap mode. *Phys. Fluids B*, 4(11):3713, 1992.

[11] W.W. Heidbrink, E.J. Strait, M.S. Chu, and A.D. Turnbull. Observation of beta-induced Alfvén eigenmodes in the DIII-D tokamak. *Phys. Rev. Lett.*, 71:855, 1993.

[12] A.D. Turnbull, E.J. Strait, W.W. Heidbrink, M.S. Chu, H.H. Duong, J.M. Greene, L.L. Lao, T.S. Taylor, and S.J. Thompson. Global Alfvén modes: Theory and experiment. *Phys. Fluids B*, 5:2546, 1993.

[13] C.Z. Cheng, L. Chen, and M.S. Chance. High-n ideal and resistive shear Alfvén waves in tokamaks. *Ann. Physics*, 161:21, 1985.

[14] L. Chen. In *Theory of Fusion Plasmas*, edited by J. Vaclavik *et al* (Bologna: SIF), p. 327, 1988.

[15] G.Y. Fu and J.W. Van Dam. Excitation of the toroidicityinduced shear Alfvén eigenmode by fusion alpha particles in an ignited tokamak. *Phys. Fluids B*, 1(10):1949, 1989.

[16] Y. Todo, M.A. Van Zeeland, A. Bierwage, and W.W. Heidbrink. Multi-phase simulation of fast ion profile flattening due to Alfvén eigenmodes in a DIII-D experiment. *Nucl. Fusion*, 54:104012, 2014.

[17] A. Bierwage, K. Shinohara, Y. Todo, and M. Yagi. Multi-time-scale energetic particle dynamics in JT-60U simulated with MHD activity, sources and collisions, poster THW/P7-39. In *Proceedings of the 25th Fusion Energy Conference, Oct 13–18, 2014, Saint Petersburg, Russia*, edited by International Atomic Energy Agency (IAEA), Vienna, 2015.

[18] Y. Todo, M.A. Van Zeeland, A. Bierwage, W.W. Heidbrink, and M.E. Austin. Validation of comprehensive magnetohydrodynamic hybrid simulations for Alfvén eigenmode induced energetic particle transport in DIII-D plasmas. *Nucl. Fusion*, 55(7):073020, 2015.

[19] Y. Todo and T. Sato. Linear and nonlinear particle-magnetohydrodynamic simulations of the toroidal Alfvén eigenmode. *Phys. Plasmas*, 5(5):1321, 1998.

[20] Y. Todo. Properties of energetic-particle continuum modes destabilized by energetic ions with beam-like velocity distributions. *Phys. Plasmas*, 13:082503, 2006.

[21] X. Wang, S. Briguglio, L. Chen, C. Di Troia, G. Fogaccia, G. Vlad, and F. Zonca. An extended hybrid magnetohydrodynamics gyrokinetic model for numerical simulation of shear Alfvén waves in burning plasmas. *Phys. Plasmas*, 18(1):052504, 2011.

[22] X. Wang, F. Zonca, and L. Chen. Theory and simulation of discrete kinetic beta induced Alfvén eigenmode in tokamak plasmas. *Plasma Phys. Control. Fusion*, 52(11):115005, 2010.

[23] X. Wang, S. Briguglio, L. Chen, C. Di Troia, G. Fogaccia, G. Vlad, and F. Zonca. Nonlinear dynamics of beta-induced Alfvén eigenmode driven by energetic particles. *Phys. Rev. E*, 86(4):045401(R), 2012.

[24] X. Wang, S. Briguglio, Ph. Lauber, V. Fusco, and F. Zonca. Structure of wave-

particle resonances and Alfvén mode saturation. *Phys. Plasmas*, 23(1):012514, 2016.

[25] F. Zonca, S. Briguglio, L. Chen, G. Fogaccia, and G. Vlad. Transition from weak to strong energetic ion transport in burning plasmas. *Nucl. Fusion*, 45(6):477, 2005.

[26] M. Azumi, G. Kurita, T. Matsuura, T. Takeda, Y. Tanaka, and T. Tsunematsu. In *Proceedings of the 4th International Symposium on Computational Methods in Applied Science and Engineering*, page 335, Paris, 1980.

[27] K. Tani, M. Azumi, H. Kishimoto, and S. Tamura. Effect of toroidal field ripple on fast ion behavior in a tokamak. *J. Phys. Soc. Japan*, 50(5):1726, 1981.

[28] A. Bierwage and K. Shinohara. Orbit-based analysis of resonant excitations of Alfvén waves in tokamaks. *Phys. Plasmas*, 21(11):112116, 2014.

[29] W. Park, S. Parker, H. Biglari, M. Chance, L. Chen, C.Z. Cheng, T.S. Hahm, W.W. Lee, R. Kulsrud, D. Monticello, L. Sugiyama, and R. White. Three-dimensional hybrid gyrokinetic-magnetohydrodynamics simulation. *Phys. Fluids B*, 4:2033, 1992.

[30] Y. Todo. Benchmark results of MEGA code for $n = 6$ TAE mode. 6th Meeting of the ITPA Energetic Particle Topical Group, Frascati/Rome, Italy, April 2011.

[31] A. Könies, S. Briguglio, N. Gorelenkov, T. Fehér, M. Isaev, P. Lauber, A. Mishchenko, D.A. Spong, Y. Todo, W.A. Cooper, R. Hatzky, R. Kleiber, M. Borchardt, G. Vlad, and ITPA EP TG. Benchmark of gyrokinetic, kinetic MHD and gyrofluid codes for the linear calculation of fast particle driven TAE dynamics. In *Proc. 24th Int. Conf. on Fusion Energy (San Diego, 2012) [ITR/P1-34]*, http://www-naweb.iaea.org/napc/physics/FEC/FEC2012/index.htm, 2012.

[32] A. Bierwage, Y. Todo, N. Aiba, K. Shinohara, M. Ishikawa, and M. Yagi. Nonlinear hybrid simulations of energetic particle modes in realistic tokamak flux surface geometry. *Plasma Fus. Res.*, 6:2403109, 2011.

[33] A. Bierwage, N. Aiba, Y. Todo, W. Deng, M. Ishikawa, G. Matsunaga, K. Shinohara, and M. Yagi. Nonlinear simulation of energetic particle modes in high-beta tokamak plasma. *Plasma Fus. Res.*, 7:2403081, 2012.

[34] A. Bierwage and K. Shinohara. Orbit-based analysis of nonlinear energetic ion dynamics in tokamaks: I. Effective mode number profile and resonant frequency tracking. *Phys. Plasmas*, 23(4):042511, 2016.

[35] A. Bierwage and K. Shinohara. Orbit-based analysis of nonlinear energetic ion dynamics in tokamaks: II. Mechanisms for rapid chirping and convective amplification. *Phys. Plasmas*, 23(4):042512, 2016.

[36] S. Briguglio, X. Wang, F. Zonca, G. Vlad, G. Fogaccia, C. Di Troia, and V. Fusco. Analysis of the nonlinear behavior of shear-Alfvén modes in tokamaks based on Hamiltonian mapping techniques. *Phys. Plasmas*, 21(11):112301, 2014.

[37] C.K. Birdsall and A.B. Langdon. *Plasma Physics Via Computer Simulation.* Series in Plasma Physics. Taylor & Francis Group, New York, 2005.